Title

Export of triose phosphate from the chloroplast strongly impacts photosynthetic efficiency and intracellular ROS accumulation in Chlamydomonas

Weichao Huang (黄伟超)[1]†*, Anagha Krishnan[2]†, Anastasija Plett[3], Michelle Meagher[4], Nicole Linka[3], Yongsheng Wang[1,5], Bijie Ren[1], Justin Findinier[1], Petra Redekop[1], Neda Fakhimi[1], Rick G. Kim[1], Devin A. Karns[2], Nanette Boyle[4], Matthew C. Posewitz[2], Arthur R. Grossman[1]*

[1]Department of Plant Biology, Carnegie Institution for Science, Stanford, CA 94305, USA

[2]Department of Chemistry, Colorado School of Mines, Golden, CO 80401, USA

[3]Institute of Plant Biochemistry, Heinrich-Heine University Düsseldorf, 40225 Düsseldorf, Germany

[4]Department of Chemical and Biological Engineering, Colorado School of Mines, Golden, CO 80401, USA

[5]School of Life Sciences, Tsinghua University, 100084 Beijing, China

†Authors contributed equally.

*Corresponding Author: Weichao Huang; Address: The Carnegie Institution for Science, 260 Panama St. Bldg. 100; Stanford, CA 94305; email: whuang@carnegiescience.edu

*Corresponding Author: Arthur R. Grossman; Address: The Carnegie Institution for Science, 260 Panama St. Bldg. 100; Stanford, CA 94305; email: agrossman@carnegiescience.edu

Abstract

Modulation of the rates of export of photoassimilates from the chloroplast is essential for controlling the distribution of fixed carbon in the cell and maintaining optimum photosynthetic rates. Additionally, the export of carbon metabolites from the chloroplast can serve in the transduction of chloroplast signals to the nucleus in response to stressful environmental conditions. In this study we identified triose phosphate/phosphate translocators 2 and 3 (CreTPT2 and CreTPT3) in the green alga *Chlamydomonas reinhardtii* (Chlamydomonas throughout) that exhibited similar substrate specificities but were differentially expressed over the diel cycle. We focused mostly on analyzing CreTPT3 because of its high level of expression and the severe phenotype exhibited by *tpt3* relative to *tpt2* mutants. Null mutants for CreTPT3 had a pleiotropic phenotype that impacted growth, photosynthetic activities, metabolite profiles, carbon partitioning, and organelle-specific accumulation of H_2O_2. These analyses demonstrated that CreTPT3 is a dominant conduit on the chloroplast envelope for the transport of photosynthetically fixed carbon. In addition, CreTPT3 can serve as a safety valve that moves excess reductant out of the chloroplast, which helps stabilize the plastid redox state. Finally, CreTPT3 appears to be essential for preventing the cells from experiencing extreme oxidative stress and the accumulation of reactive oxygen species, even under low/moderate light intensities. Our studies also suggest that there are differences in the export of photoassimilates from the chloroplasts of Chlamydomonas and vascular plants and that there has been subfunctionalization of CreTPT transporters in the former.

Introduction

Photosynthetic organisms can absorb excess, potentially damaging levels of light energy during mid-day (when photosynthetic electron transport becomes saturated) and can suffer from extreme damage, especially when experiencing rapid fluctuations in light intensities or when subjected to nutrient limiting conditions and other environmental stresses that impair the productive utilization of excitation energy (Chaux et al., 2017; Saroussi et al., 2017). To cope with excess excitation energy, plants and algae have evolved mechanisms to dissipate this energy through nonphotochemical quenching (NPQ). The excess reductant and energy can also be eliminated by photochemical quenching. While the dominant form of photochemical quenching often involves the use of the electrons/reductant to fix inorganic carbon (Ci), which is directed toward growth or stored in the form of starch and lipids (Krishnan et al., 2015; Ge et al., 2014; Huang et al., 2018), redox equivalents can also be trafficked to other outlets where they are not used for anabolic processes. The main alternative photochemical electron outlets involve the reduction of O_2 to H_2O in H_2O-to-H_2O cycles that include a (*i*) Mehler-type reaction that is noncatalytic and functions on the acceptor side of PSI, (*ii*) flavodiiron protein reactions (Jokel et al., 2018) (FLVs, NADPH:flavin oxidoreductase) that catalytically reduce O_2 on the acceptor side of PSI without generating reactive oxygen species (ROS), (*iii*) the plastid terminal oxidase (Houille-Vernes et al., 2011) (PTOX, plastoquinol: oxygen oxidoreductase) reaction that can use electrons from the PQ pool to reduce O_2, and (*iv*) the movement of redox equivalents from the chloroplast to the mitochondrion where they can be used to reduce O_2 through various electron transport activities.

Mechanisms also exist in which fixed carbon and reducing equivalents can be shuttled between the chloroplast and cytoplasm. Studies with *Arabidopsis thaliana* revealed that the malate shuttle, which involves multiple malate dehydrogenases (MDH) and malate/OAA translocators (OMT), functions in the export of reductant from the chloroplast and the management of redox conditions in the chloroplast (Zhao et al., 2020, 2018). In addition to the malate shuttle, the triose phosphate (triose-P)/phosphate (Pi) translocator (TPT) has been proposed to be involved in moving fixed carbon out of the chloroplast, but can also act as a safety valve for eliminating excess reducing power from the chloroplast (Fliege et al., 1978; Flügge et al., 1989; Lee et al., 2017b; Stocking and Larson, 1969; Raghavendra and Padmasree, 2003; Johnson and Alric, 2013). The synthesis of triose-Ps during photosynthetic CO_2 fixation by the Calvin-Benson-Bassham Cycle (CBBC) is supported by the reducing power/energy (NADPH, ATP) derived from photosynthetic electron

75 transport.

76 The TPTs reside on the inner chloroplast envelope membrane and can transport triose-Ps
77 (glyceraldehyde 3-phosphate (GAP), dihydroxyacetone phosphate (DHAP)) and the three carbon
78 acid 3-phosphoglycerate (3-PGA) in a counter exchange for cytosolic Pi (Fliege et al., 1978; Lee
79 et al., 2017a; Flügge et al., 1989). These transporters belong to a family of plastidic phosphate
80 translocators (pPTs) that function as antiport systems involved in exchanging Pi with
81 phosphorylated C3, C5 or C6 compounds (Flügge et al., 2003). Most angiosperms have two *TPT*
82 genes in their genome, except for various monocots and two dicot families, the Amaranthaceae
83 and the Brassicaceae, which have a single *TPT* gene (Bockwoldt et al., 2019). In plants, cytosolic
84 trioses exported from the chloroplast by the TPTs are used for the biosynthesis of sucrose and
85 other metabolites (Riesmeier et al., 1993) and to drive respiratory activity. In addition to TPTs,
86 plants harbor the three other pPT subfamilies (Fischer et al., 1997; Kammerer et al., 1998; Eicks
87 et al., 2002; Lee et al., 2017b; Flügge et al., 1989). These include the glucose 6-phosphate (Glc6P)
88 translocator (GPT), which imports Glc6P into plastids in heterotrophic tissue (Fischer et al., 1997;
89 Kammerer et al., 1998; Eicks et al., 2002; Lee et al., 2017b; Flügge et al., 1989), the xylulose
90 phosphate translocator (XPT), which plays a key role in coordinating the cytosolic and plastidic
91 pentose phosphate pathways (Fischer et al., 1997; Kammerer et al., 1998; Eicks et al., 2002; Lee
92 et al., 2017b; Flügge et al., 1989), and the phosphoenolpyruvate (PEP) translocator (PPT), which
93 imports PEP into C3 plastids; the PEP can be used for the synthesis of fatty acids, as substrate for
94 the shikimate pathway (Streatfield et al., 1999; Prabhakar et al., 2010) and for the export of PEP
95 in C4 plants (Häusler et al., 2000).

96 Over the last few decades, the physiological functions of the TPTs have been examined in some
97 detail. Various plants do not exhibit a strong phenotype if the chloroplast TPT is either eliminated
98 or its level is reduced (Häusler et al., 1998; Walters et al., 2004; Schneider et al., 2002; Riesmeier
99 et al., 1993). A reduction in TPT activity can be compensated for by diverting assimilated carbon
100 into a transitory starch pool that is subjected to accelerated turnover in the light and/or dark
101 (Häusler et al., 1998; Walters et al., 2004; Riesmeier et al., 1993), leading to accumulation of starch
102 degradation products that can be exported from the chloroplast and used in other cellular
103 compartments. Interestingly, a deficiency of the TPT in rice, a plant that uses sucrose stored in the
104 leaves as its major transitory form of fixed carbon, led to severe phenotypic consequences; the
105 plants exhibited reduced photosynthetic rates and decreased levels of both starch and soluble

106 sugars relative to wild type (WT) plants (Lee et al., 2014).

107 Microalgae have high photosynthetic conversion efficiencies, can thrive in fresh to hypersaline
108 waters and can be metabolically versatile. They have also attracted considerable interest worldwide
109 because of their ability to synthesis large quantities of lipids (e.g. for biofuels and food products),
110 starch, pigments and other bioproduction, and can serve in the remediation of waste water (Khan
111 et al., 2018; Bhatt et al., 2022). The transporters used for moving photoassimilate between the
112 chloroplast and other cellular compartments and the mechanisms and regulation of these
113 transporters in microalgae have not been extensively explored. Developing a more informed
114 understanding of central metabolism in microalgae and the movement of metabolites among
115 compartments can enable additional work on the establishment, regulation, and evolution of
116 metabolic networks in algae and the ways in which algae can be tailored for production purposes
117 and for sustained growth under specific environmental conditions.

118 There are still relatively few studies that explore the functionalities of the TPTs and other pPTs in
119 single-celled photosynthetic organisms (some in red algae, green algae, cryptophytes), which are
120 often based on in vitro activities of these proteins in liposome transport assays (Moog et al., 2020;
121 Haferkamp et al., 2006; Linka et al., 2008). Active transport of triose-P has been noted multiple
122 times in Chlamydomonas (Klöck and Kreuzberg, 1991; Boschetti and Schmid, 1998). Based on
123 phylogenetic analysis of pPTs, the green algae Chlamydomonas contains one potential TPT, two
124 PPTs and one GPT/XPT. However, the physiological functions of the pPTs in this alga have not
125 been characterized.

126 In this study, we used Chlamydomonas, the well-established model green algal system that has
127 been extensively used to analyze various physiological processes, to dissect the function of
128 chloroplast TPTs. Chlamydomonas contains more than 30 TPT homologs; the informatic analyses
129 of these proteins are still not refined enough to be certain of their substrate specificities and, in
130 many cases, the transported metabolites are likely not triose-Ps. Of the four putative pPTs, we
131 discovered that Chlamydomonas contains two TPTs (CreTPT2 and CreTPT3) based on yeast
132 liposome transport assays. CreTPT2 was previously reported to be a PPT based on phylogenetic
133 analysis. These two TPTs exhibited sub-functionalization that is reflected by their expression
134 levels and temporally and environmentally distinct regulatory patterns. Due to the severer
135 phenotypes exhibited by *tpt3* relative to *tpt2* mutants, we focused our analyses on Chlamydomonas

136 TPT3 (CreTPT3) which, among the four predicted pPTs, is highly expressed in the light and
137 strongly induced by various environmental stresses. Through a series of physiological analysis, we
138 demonstrated that CreTPT3 is a major conduit on the chloroplast envelope for the trafficking of
139 fixed carbon, sustaining central carbon metabolism, dissipating excess energy, enabling high rates
140 of photosynthetic electron transport, preventing intracellular hydrogen peroxide (H_2O_2)
141 accumulation, and balancing redox conditions at the subcellular level.

142 **Results**

143 **The triose-P/Pi translocator (DMT/TPT) family**

144 Candidate genes encoding triose-P/Pi transporters (TPT) of Chlamydomonas were identified by
145 blasting the Arabidopsis TPT protein (AT5G46110.1) against proteins encoded on the
146 Chlamydomonas genome. The TPT family is the largest within the drug/metabolite transporter
147 (DMT) superfamily in eukaryotes and includes triose-P and sugar-phosphate transporters
148 associated with chloroplasts; many of the family members are still not functionally characterized
149 (Jack et al., 2001; Knappe et al., 2003; Weber et al., 2006). We have identified 32 genes encoding
150 potential TPTs in the version v6.1 genome of Chlamydomonas, with four members, CreTPT10
151 (CreTPT1 in v5.6 genome), CreTPT2 (CreTPT2 in v5.6 genome), CreTPT3 and CGL51
152 (CreTPT25 in v5.6 genome), predicted to have a transit peptide that would localize the protein to
153 the chloroplast (**Supplementary Table 1**). These four candidates were included in a phylogenetic
154 analysis of plant and algal pPTs that showed that CreTPT3 is a putative TPT, CreTPT2 and
155 CreTPT10 are putative PPTs, and CGL51 is a putative GPT or XPT (Bockwoldt et al., 2019).

156 To examine the potential substrate specificities of the four putative pPTs, their amino acid
157 sequences were aligned with pPTs from Arabidopsis (AtPTs) (**Supplementary Fig. 1A**). The
158 ability of these transporters to use triose-P/DHAP or 3-PGA as substrate is dependent on five
159 highly conserved amino acid residues (H184, K203, Y338, K359, and R360 in AtTPT1) (Lee et
160 al., 2017b; Moog et al., 2020). Of the putative pPTs in Chlamydomonas, only CreTPT3 and
161 CGL51 contain all five of these residues (H170, K189, Y322, K345, and R346 in CreTPT3)
162 (**Supplementary Fig. 1A**). In AtTPT1, residue F262 (F248 in Chlamydomonas in the analogous
163 protein, CreTPT3) is thought to inhibit PEP access to the binding site; this residue is replaced by
164 N in AtPPT1 (PPT) (Lee et al., 2017b; Moog et al., 2020). CGL51 has an M at position F248,
165 indicating that unlike CreTPT3, CGL51 might have preference for other substrates. Moreover,

166 protein sequence similarity and identity analysis show CreTPT3 and CreTPT2 share the highest
167 and the second highest similarity and identity with AtTPT1, (**Supplementary Fig. 1B**) and are 57%
168 and 49 % similar to AtTPT1, respectively.

169 **CreTPT2 and CreTPT3 transport properties**

170 We defined the subcellular localization and substrate preferences of both CreTPT2 and CreTPT3.
171 As shown in **Fig. 1A**, both CreTPT2 and CreTPT3 fused to VENUS localized to the chloroplast
172 envelope. To evaluate the substrate specificity of these transporters, each of them was expressed
173 in *Saccharomyces cerevisiae* (yeast) and the resulting recombinant protein was biochemically
174 analyzed using a liposome uptake assay. The Cre*TPT2* and Cre*TPT3* genes were fused at their C
175 termini to a sequence encoding a his tag, codon-optimized, and expressed in yeast (**Fig. 1B**), and
176 total cell membranes were isolated and reconstituted into liposomes (Loddenkötter et al., 1993;
177 Linka et al., 2008). Chloroplast phosphate transporters in vascular plants can catalyze a Pi/Pi
178 homo-exchange in vitro. Both CreTPT2 and CreTPT3 reconstituted in liposomes were able to
179 catalyze the signature Pi homo-exchange, whereas in the absence of a counter-exchange substrate,
180 little Pi uptake was detected (**Fig. 1C** and **D**, left). In contrast, very low Pi uptake rates were
181 observed for liposomes reconstituted with membranes from yeast cells lacking CreTPT2 or
182 CreTPT3 (**Supplementary Fig. 2**), indicating that the introduced transporters were responsible for
183 the detected Pi import activity in the yeast liposomes.

184 To assess the substrate specificity of the CreTPT transporters, the initial rates of Pi uptake into
185 liposomes preloaded with saturating concentrations (30 mM) of various potential counter-
186 exchange substrates were determined. As the right panels of **Fig. 1C** and **D** show, both CreTPT2
187 and CreTPT3 exhibited the highest activity when DHAP was used as the substrate for the yeast
188 liposome assay. For both transporters, the relative initial velocity for DHAP/Pi exchange was
189 slightly higher than that of 3-PGA/Pi (the relative 3-PGA/Pi exchange was 75% of DHAP/Pi
190 exchange) while Pi uptake into liposomes preloaded with PEP was much lower (**Fig. 1C** and **D**,
191 right panels). Pi import was negligible when CreTPT2 or CreTPT3 liposomes were preloaded with
192 Glc-6-P, Glc-1-P, Fru-6-P, and Gal-1-P (**Fig. 1C** and **D**, right panels). These results show that
193 CreTPT2 and CreTPT3 have almost the same substrate preferences, with both specifically
194 catalyzing the transport of triose-P and 3-PGA across the membrane in exchange for Pi.

195 Characterizations of the K_M and K_i for CreTPT2 and CreTPT3 were performed to determine the

196 affinity of these transporters for the various substrates. CreTPT3 has an apparent Michaelis-
197 Menten constant (K_M) of 1.1 +/- 0.2 mM for Pi (**Fig. 1E**), which is comparable to the value
198 obtained for the vascular plant TPT ortholog (Fliege et al., 1978). CreTPT2 has a slightly lower
199 K_M for Pi than CreTPT3 (0.77 +/- 0.05 mM) (**Fig. 1E**). However, while the 3-PGA Ki values were
200 comparable for the two transporters, DHAP was more effective in inhibiting the CreTPT3-
201 dependent Pi exchange than CreTPT2-dependent Pi exchange (**Fig. 1E**). These results suggest that
202 CreTPT3 may has a greater specificity for the transport of DHAP than CreTPT2 and that it may
203 be more effective in transporting C3 phosphorylated compounds than CreTPT2. In the case of
204 PEP, no inhibition of the Pi/Pi homo-exchange was observed, even at the non-physiologically high
205 concentration of 5 mM. Overall, the results of these in vitro assays indicate that both CreTPT2 and
206 CreTPT3 have a typical plant-TPT substrate spectrum (Fliege et al., 1978) and can transport Pi,
207 triose-P (DHAP) and 3-PGA in a counter-exchange mode. However PEP might not be a
208 physiologically relevant substrate for either CreTPT2 or CreTPT3, as was shown for apoplast TPT
209 homologues in other organisms (Lim et al., 2010; Moog et al., 2020). Furthermore, the values
210 generated in these analyses may not precisely reflect transport kinetics in vivo since the two
211 transporters used for these in vitro assays were fused to a His-tag at their N terminus, and the yeast
212 liposomes would have a different lipid composition than the chloroplast inner envelop membrane,
213 where these transporters are normally localized.

214 **Isolation of *tpt2* and *tpt3* null mutants of Chlamydomonas and their impacts on cell growth**

215 To explore the role of CreTPT2 and CreTPT3 in trafficking carbon and potentially reductant across
216 the chloroplast envelope in vivo, CRISPR knockouts of Cre*TPT2* or Cre*TPT3* were generated. We
217 used the CRISPR-Cas9 editing system to disrupt the Cre*TPT2* or Cre*TPT3* genes while at the same
218 time integrating the hygromycin marker gene (*AphVII*) into the edited site (**Fig. 2A,**
219 **Supplementary Fig. 3** and **4**). Two independent knockouts of Cre*TPT2* (*t2ko1* and *t2ko2*) were
220 obtained, with the marker gene inserted into exon 8 (**Fig. 2A)**; the transcript abundances of
221 Cre*TPT2* were significantly reduced in these two edited strains (**Fig. 2B**). Three independent
222 knockouts of Cre*TPT3* were obtained, including *t3ko1*, with the marker gene inserted into exon 1,
223 and *t3ko2* and *t3ko3*, with the marker gene inserted into exon 7; no CreTPT3 protein was detected
224 in any of these edited strains (**Fig. 2B**).

225 To elucidate the physiological roles of CreTPT2 and CreTPT3, we first examined growth of the

226 parental WT strain and the knockout mutants under either low light (LL, 30 µmol photons m^{-2} s^{-}
227 ^{1}), moderate light (ML, 250-300 µmol photons m^{-2} s^{-1}) or high light (HL, 450 µmol photons m^{-2} s^{-}
228 ^{1}). The design of the experiments in which the cells were transferred from one light condition to
229 another is shown in **Supplementary Fig. 5**. The two *tpt2* mutants (*t2ko1* and *t2ko2*) were not
230 impacted by growth in LL, but their growth was significantly impaired relative to WT cells under
231 HL on either photoautotrophic (TP) or heterotrophic (TAP) solid agar medium (**Fig. 2C**). In
232 contrast, the Cre*TPT3* mutants (*t3ko1, t3ko2* and *t3ko3*) exhibited severe growth impairment even
233 in LL, and completely stopped growing under ML and HL, on either TP or TAP agar medium (**Fig.**
234 **2C, D**). Due to the striking growth phenotypes caused by the loss of CreTPT3, we focused on
235 investigating the physiological functions of TPT3 by analyzing *tpt3* mutants in more detail in this
236 study. The differences in transcript changes between Cre*TPT2* and Cre*TPT3* under various
237 environmental conditions were examined and are described in the 'Discussion' section.

238 Growth curves were also determined for WT and *tpt3* mutant cells in liquid medium (TP) in LL,
239 ML and HL (**Fig. 2E** and **2F**); the results were in accord with those observed for the solid medium
240 growth assays. Additionally, *tpt3* mutant cells in both LL and ML exhibited an increased cell
241 diameter and formed clusters of cells that appear to be less able to separate following cell division
242 (**Supplementary Fig. 6A**, **B**). To further confirm that the growth phenotypes are a consequence
243 of the *tpt3* knockout, we introduced a wild-type copy of Cre*TPT3* fused to VENUS into the mutant
244 strains (**Fig. 2B**, right). As shown in **Fig. 2D-G**, ectopic expression of the wild-type Cre*TPT3* in
245 the *t3ko2* mutant (*C_T3KO2*) rescued the reduced growth phenotype of the mutant under all light
246 conditions tested in this study (LL/ML/HL).

247 We also analyzed the chlorophyll content of photoautotrophically grown cells after transferring
248 them from LL to ML and found that *t3ko2* had reduced chlorophyll content relative to WT cells
249 after 24 h in ML (**Fig. 2F-G** and **Supplementary Fig. 7**). Cell numbers and total chlorophyll were
250 quantified following the LL to ML transition. The chlorophyll levels per cell declined in all strains
251 at 24 and 48 h following transfer to ML; however, it was lower by approximately half in *t3ko2*
252 (0.34 µg/10^6 cells) relative to either WT cells or the *C_T3KO2* rescued strain (both ~0.72 µg/10^6
253 cells) after 24 h of ML (**Supplementary Fig. 7**), with some additional increase in cell density for
254 WT and *C_T3KO2* after 48 h of ML (which might result in some shading). Finally, when mutant
255 cells were transferred to HL for 24 h they became strongly bleached (**Fig. 2F**).

256 Taken together, these results indicate that the activity of the CreTPT3 transporter is essential for
257 optimal growth over a range of light intensities (LL/ML/HL).

258 **The *tpt3* mutant exhibits hyper-accumulation of 'storage' carbon**

259 To explore the impact of the loss of CreTPT3 activity on carbon partitioning, we quantified carbon
260 storage (starch and lipids) following a transition of WT and the *t3ko2* mutant from LL to ML.
261 Lugol staining showed extensive starch accumulation in the *t3ko2* cells after a 48-h exposure to
262 ML, whereas WT cells were barely stained (**Fig. 3B**). Furthermore, as shown in **Fig. 3A**, there is
263 a ~55-fold difference in the level of starch that accumulated in *t3ko2* relative to WT cells (13.29
264 compared to 0.24 µg starch/µg chlorophyll, respectively) after 24 h of illumination in ML. The
265 mutant also accumulated ~24-fold more lipid than WT and *C_T3KO2* cells (on a chlorophyll basis),
266 as monitored by Nile Red fluorescence, over the same time period (WT and *t3ko2*: 1038 and 41
267 Nile Red fluorescence/chlorophyll, respectively) (**Fig. 3C, D**). Since the chlorophyll in the mutant
268 on a per cell basis was approximately 50% relative to that of WT cells after 24 h in ML, the
269 accumulated starch and lipid on a per cell basis would be ~25-fold more starch and ~12-fold more
270 lipid in the mutant relative to the WT strain. Additionally, mutant cells are much larger and tended
271 to exhibit more aggregation than WT cells (**Supplementary Fig. 6A, B**). These results suggest
272 that the inability to transport triose-P between the chloroplast and the cytosol through CreTPT3
273 resulted in a repartitioning of photosynthetic assimilates (carbon, reductant, and ATP) toward the
274 synthesis of both starch and neutral lipid.

275 **Cre*TPT3* deletion leads to accumulation of CBBC/glycolytic/gluconeogenic intermediates**

276 To understand the metabolic consequences of the loss of CreTPT3 on growth under LL and ML,
277 comparative metabolite analyses of WT and the *t3ko2* mutant were performed on cells grown in
278 LL and after shifting them to ML for both 45 min and 6 h. As mentioned above, the level of starch
279 increased dramatically in the mutant relative to WT cells (**Fig. 3A, B** and **Supplementary Fig.**
280 **8A**). Pool sizes of various central carbon metabolites, particularly those of the
281 CBBC/glycolysis/gluconeogenesis pathways and intermediates of the TCA/glyoxylate cycle (**Fig.**
282 **3F**), were quantified. Data was normalized to both chlorophyll content (**Fig. 3E**) and cell number
283 (**Supplementary Fig. 8B**). The fold-change in the quantity of each metabolite in the mutant
284 relative to WT under LL or at 45 min and 6 h after the switch to ML is given in **Fig. 3G** and
285 **Supplementary Fig. 8C**.

286 At the time of shifting cells from LL (**Fig. 3E**, time 0 h) to ML, the *t3ko2* mutant had already
287 accumulated a significantly larger pool (2- to 6-fold) of glycolytic/gluconeogenic intermediates
288 [DHAP, 3-PGA and FBP (all three shared with CBBC), G6P, PEP] and of some metabolites of the
289 CBBC pathway (E4P, RU5P/X5P, R5P) compared to WT cells, suggesting that the loss of
290 CreTPT3 resulted in a back-up of these metabolites within the cell; our hypothesis is that these
291 metabolites are accumulating in the chloroplast stroma due to the reduced ability of the mutant
292 chloroplast to export fixed carbon, which is supported by the observed accumulation of starch and
293 TAG in the mutant strain (**Fig. 3A-D** and **Supplementary Fig. 8A**). While the pool sizes of
294 fumarate and malate (metabolites of the TCA/glyoxylate cycle) were similar in both strains under
295 LL, following the transition of the cells to ML, WT cells exhibited a significant increase in the
296 pool sizes of those metabolites while the mutant maintained a lower level, indicating that the loss
297 of CreTPT3 either directly (by supplying precursors) or indirectly (metabolic rewiring) impacts
298 their levels.

299 Thus, a primary function of CreTPT3 appears to be the export of photosynthetically synthesized
300 reduced carbon, which would drive metabolic processes in the cytoplasm and other cellular
301 compartments, such as the mitochondrion, while enabling the import of Pi into the chloroplast,
302 which sustains ATP synthesis.

303 **The *tpt3* mutant has reduced photosynthetic activity when grown in ML**

304 To understand the impact of the loss of CreTPT3 activity on PET, we quantified photosynthetic
305 activities following a transition from LL to ML (**Supplementary Fig. 5**). Photosynthetic O_2
306 evolution rates (OERs) were measured for WT, *t3ko2* and *C_T3KO2* over a range of light
307 intensities. LL acclimated WT, *t3ko2*, and *C_T3KO2* showed comparable OERs at intensities
308 below 200 μmol photons m^{-2} s^{-1}, while at saturating light intensities of ≥600 μmol photons m^{-2} s^{-1},
309 the OER of *t3ko2* was diminished slightly relative to the WT and the complemented strain (**Fig.**
310 **4A**). Upon acclimation of the cells to ML for 24 h, the *t3ko2* mutant consistently displayed lower
311 OERs than WT cells or *C_T3KO2* under all actinic light intensities used (**Fig. 4A**). Additionally,
312 while the Fv/Fm in the mutant grown in LL was comparable to that of WT and *C_T3KO2* (**Fig.**
313 **4B**), after exposure of the mutant cells to ML for 6 h, the Fv/Fm declined to about 50% of the WT
314 and *C_T3KO2* levels; the decline in the mutant continued over a period of 24 h in ML, with a 3-
315 fold decrease in Fv/Fm for *t3ko2* compared to that of WT cells (**Fig. 4B**). These results indicate

316 that damage to PSII reaction centers occurs following exposure of the mutant to ML.

317 To examine the redox state of the photosynthetic apparatus, the pool of electron acceptors
318 downstream of PSII were evaluated. We quantified the photochemical efficiency (qL) of all strains
319 at various light intensities after growth in LL or shifting them to ML for 6 and 24 h (**Fig. 4C**). The
320 photosynthetic parameter qL indicates the redox state of Q_A, the primary electron acceptor of the
321 PSII reaction center. Assuming that Q_A and Q_B are in equilibrium, qL would reflect the redox
322 status of the PQ pool; a lower qL value indicates a more reduced electron transport chain (Kramer
323 et al., 2004). 1-qL positively correlates with the PQ pool redox state. In the LL-acclimated cells,
324 1-qL was significantly higher in *t3ko2* even at low levels of actinic illumination compared to that
325 of WT cells and the rescued strain. For cells that had been acclimated to ML (6 h and 24 h), 1-qL
326 was 70% of the near maximum value for *t3ko2*, even under relatively low actinic light conditions
327 (e.g. 100 µmol photons m^{-2} s^{-1}), indicating a highly reduced PQ pool. In contrast, for WT and the
328 complemented strain at the same light intensity, the 1-qL value attained only ~20% of the
329 maximum value (**Fig. 4C**). These results suggest that the PQ pool is much more reduced in LL-
330 acclimated *t3ko2* relative to WT and *C_T3KO2* (**Fig. 4C**), and that there is a much more
331 pronounced reduction of this pool at all actinic light intensities in ML grown *t3ko2* mutants. These
332 results suggest a limitation in electron flow downstream of the PQ pool in both LL and ML grown
333 *t3ko2*.

334 Moreover, we analyzed how fast PET becomes restricted following the transfer of LL-grown *t3ko2*,
335 *C_T3KO2* and WT cells to HL (400-450 µmol photons m^{-2} s^{-1}) by monitoring changes in the redox
336 state of the PQ pool. We observed that the PQ pool in *t3ko2* began to be more reduced than that of
337 WT cells and *C_T3KO2* after 105 s of elevated illumination (**Fig. 4D**), and that this was even more
338 pronounced at longer times in HL. These results suggest that PET can be rapidly limited by
339 diminished triose-P export from the chloroplast; elimination of CreTPT3 has a strong impact on
340 PET activity.

341 To determine if PSI was also impacted in the mutant cells, we analyzed PSI/P700
342 oxidation/reduction kinetics following exposure of LL-grown cells to ML in the presence of
343 DCMU (20 µM) and hydroxylamine (1 mM) to block a contribution of electrons from PSII. Levels
344 of photo-oxidizable P700 following exposure to actinic light for 5 sec were similar in all LL-
345 acclimated strains (**Fig. 4E**). However, the level of photo-oxidized P700 in ML-acclimated cells

346 declined in the mutant to ~40-50% of that in WT and *C_T3KO2* cells (**Fig. 4E**), indicating that
347 PSI is more reduced in the *t3ko2* mutant after ML exposure. As shown in **Fig. 4F**, the oxidation
348 rate of P700 following a dark to light transition was much slower in the ML-acclimated *t3ko2*
349 compared to that of WT. These results suggest that the mutant has a diminished level of available
350 electron acceptors on the acceptor side of PSI (relative to WT and *C_T3KO2*) after growth in ML.

351 **CreTPT3 inactivation dramatically affected accumulation and distribution of cellular H_2O_2**

352 To investigate the relationship of CreTPT3 activity to oxidative stress, we assayed ROS production
353 in the mutant using the fluorescent probe CM-H2DCFDA, which upon exposure to increasing
354 ROS levels is converted to the green-fluorescent molecule dichlorofluorescein (DCF). DCF
355 fluorescence was visualized by confocal microscopy. As shown in **Fig. 5A** and **B**, ROS levels in
356 the *t3ko2* mutant were markedly increased (~3-fold) after 48 h in ML, while little difference in
357 ROS levels was detected in WT cells.

358 For an alternative, dynamic method for evaluating redox changes in the chloroplast, we used the
359 redox sensitive green fluorescent protein roGFP2, which was targeted to the chloroplast stroma
360 (**Fig. 5C**, upper panel) and mitochondrion (**Fig. 5C**, lower panel). roGFP2 monitors ratiometric
361 redox changes of glutathione, which reflects cellular ROS levels (Dorion et al., 2021; Vevea et al.,
362 2013). LL-acclimated WT cells and the *t3ko2* mutant exhibited similar levels of chloroplast
363 roGFP2 oxidation (**Fig. 5D**). Upon transfer of these cells to ML, the mutant showed an increase in
364 chloroplast oxidative conditions, with a 5.0-fold increase after 1.5 h, and a 2.0-fold increase after
365 6 h, which is 1.8- and 1.6-fold higher than the values measured in WT cells (**Fig. 5D**). Additionally,
366 as triose-P is exported to the cytosol by CreTPT3, it could potentially be further metabolized and
367 donate redox equivalents to the mitochondrial electron transport chain and alter mitochondrial
368 ROS production. Therefore, we also measured mitochondrial redox levels at different light
369 intensities in both WT and the *t3ko2* mutant using the roGFP2 sensor targeted to the mitochondrion.
370 Upon a LL to ML shift for 1.5 and 6.0 h, neither WT nor *t3ko2* displayed a significant change in
371 fluorescence from the mitochondrial targeted roGFP (**Fig. 5E**). These results suggest that the
372 mitochondrial redox level is maintained after shifting either LL acclimated WT or *t3ko2* cells to
373 ML. Overall, the inability to export triose-P through CreTPT3 markedly increased the level of
374 oxidative stress in the chloroplast but not in the mitochondrion.

375 We also determined if the ROS accumulated in *t3ko2* is H_2O_2 and whether this molecule shows

differential accumulation in the different subcellular compartments; the analysis was based on the use of a hypersensitive sensor of H_2O_2, roGFP2-Tsa2ΔCR, which was previously used for studies with Chlamydomonas (Niemeyer et al., 2021). In this analysis, we monitored real-time accumulation of H_2O_2 in the stroma, cytosol, mitochondrion, and nucleus (**Fig. 6A**) following a 20 min exposure of the cells to either HL or very low light (**Fig. 6B-E**). The *t3ko2* stromal H_2O_2 level increased within 2.5 min of the light exposure and attained a 1.4-fold increase after 20 min of illumination with HL compared to the initial level in LL (**Fig. 6B**). The stromal H_2O_2 levels in WT cells showed little change after being shifted to HL, however, the level declined when the cells were shifted to 10 μmol photons m^{-2} s^{-1}, or very low light. Notably, after 20 min in HL, the stroma of the *t3ko2* mutant accumulated ~1.6-fold more H_2O_2 than that of the WT cells; *t3ko2* mutant cells in very low light accumulated a similar amount of stromal H_2O_2 as WT cells after exposure to HL (**Fig. 6B**). The cytosolic probe also responded rapidly, with a 1.2-fold increase for WT and a 1.4-fold increase for the *t3ko2* mutant (**Fig. 6C**); note that the initial levels of H_2O_2 prior to the transfer of the cells to HL or very low light were much lower in the WT cells than in the mutant. The *t3ko2* cytosolic H_2O_2 level was elevated relative to the level in WT cells by 2.1-fold after 20 min of illumination in HL (**Fig. 6C**). We did not observe a significant change in H_2O_2 levels in the mitochondrion for either the WT or the *t3ko2* mutant after the cells were shifted to the higher light intensity (**Fig. 6D**). Finally, the *t3ko2* mutant already accumulated much higher levels of H_2O_2 in the nucleus in LL compared to that in the WT cells, although both mutant and WT cells did not show significant changes in nuclear H_2O_2 levels after HL exposure (**Fig. 6E**).

Discussion

Cre*TPT2* and Cre*TPT3* genes exhibit different expression patterns

In this study, we discovered that Chlamydomonas contains at least two TPTs that are located on the chloroplast envelope. An earlier report suggested that CreTPT2 was a plastidic PPT (Bockwoldt et al., 2019), but based on our results, it appears to be functionally more similar to a TPT. In vitro assays show that CreTPT2 has almost the same substrate specificity as CreTPT3, although it may be less effective in DHAP/Pi exchange (**Fig. 1C-E**). To determine expression patterns of Cre*TPT2* and Cre*TPT3*, the abundance of the Cre*TPT2* and Cre*TPT3* transcripts were analyzed using RT-qPCR and by mining published RNA-seq data over the diurnal cycle, and during nitrogen/sulfur/iron starvation (Zones et al., 2015; Ngan et al., 2015; González-Ballester et

406 al., 2010; Urzica et al., 2013) (**Supplementary Fig. 9**). Cre*TPT3* was highly expressed in the light
407 and dark, with significantly higher transcript accumulation than that of Cre*TPT2* and the other
408 genes (Cre*TPT10* and *CGL51*) potentially encoding chloroplast localized pPTs (**Supplementary**
409 **Fig. 9A, C**). Cre*TPT2* and Cre*TPT3* also responded differentially to abiotic stresses. Cre*TPT3* was
410 strongly induced by nitrogen, sulfur, and iron starvation and upon exposure to HL, whereas the
411 level of the Cre*TPT2* transcript remained almost unchanged under the same conditions
412 (**Supplementary Fig. 9B-F**), suggesting that CreTPT3 plays a more pronounced role in exporting
413 triose-P from the chloroplast than CreTPT2, with potentially increasing export from the plastid
414 under HL and nutrient limitation conditions. This hypothesis is supported by the observation that
415 *tpt3* mutants displayed much more severe growth retardation relative to *tpt2* mutants upon
416 exposure to ML or HL (**Fig. 2C**, **E**). There is no evidence showing that the *TPTs* from plants are
417 induced by stress/excess absorbed excitation, and expression of the Arabidopsis *TPT* gene appears
418 to even decrease following HL exposure (Weise et al., 2019).

419 Cre*TPT2* and Cre*TPT3* exhibited distinct expression patterns over the diurnal cycle; the expression
420 of Cre*TPT2* increased rapidly after transitioning from the dark to the light, with peak accumulation
421 after one hour in the light, when the transcript level of Cre*TPT3* was at its lowest (**Supplementary**
422 **Fig. 9A**). Continued exposure to light led to a decrease in the level of the Cre*TPT2* transcript to
423 near zero while the transcript from Cre*TPT3* steadily increased in the light, reaching a peak in mid-
424 day (**Supplementary Fig. 9A**). The Cre*TPT2* expression pattern suggests that it might play a role
425 in exporting triose-P at the beginning of light period, when the light intensity and photosynthesis
426 are low and low levels of triose-P would be synthesized in the stroma. As the light intensity
427 increases over the course of the day, higher levels of triose-P are synthesized and its trafficking
428 out of the chloroplast for use in other subcellular compartments would likely predominantly
429 involve the activity of CreTPT3. The greater specificity of CreTPT3 than CreTPT2 for transporting
430 DHAP (**Fig. 1E**) may make it more effective than CreTPT2 in transporting C3 phosphorylated
431 compounds. This possibility is congruent with the finding that there is elevated
432 synthesis/accumulation of CreTPT3 mRNA during the day when the light intensity reaches its
433 peak (Zones et al. 2015) and there would be rapid synthesis of the C3 phosphorylated compounds.
434 Overall, the subfunctionalization of the two Chlamydomonas triose-P transporters based on their
435 expression levels, patterns of RNA accumulation over the course of the day and upon nutrient

436 deprivation, and their substrate specificities, may help tune the export of triose-P from the
437 chloroplast with respect to the diurnal cycle and dynamic environmental cues.

438 **CreTPT3 also serves as a redox valve, transferring reductant to the cytoplasm**

439 It was previously proposed that chloroplast TPTs could catalyze two potential reactions in the light
440 (**Fig. 7**) based on the crystal structure of the red algal TPT (Lee et al., 2017b) and in vitro assays
441 using isolated spinach chloroplasts (Stocking and Larson, 1969); both triose-P/Pi, and triose-P/3-
442 PGA exchange across the chloroplast inner envelope membrane. The former reaction can route
443 both carbon skeletons and reductants into the cytoplasm while importing Pi back into the
444 chloroplast for ATP regeneration. The latter reaction would import 3-PGA into the chloroplast in
445 exchange for triose-P (DHAP, GAP), which would serve to transfer reductant from the chloroplast
446 to the cytosol while transferring 3-PGA back into the chloroplast where it can be reduced by the
447 CBBC and stimulate the regeneration of ribulose 1,5-bisphosphate. Indeed, in vitro, CreTPT3 can
448 actively transport both triose-P and 3-PGA in exchange for Pi (**Fig. 1**), indicating that this
449 transporter can serve as both a carbon and 'reductant shuttle' which would help sustain
450 photosynthetic electron flow.

451 Studies of photosynthetic activities and growth of WT and *tpt3* mutants (e.g. *t3ko2*) in LL, ML
452 and HL support the idea that the mutant is highly compromised in its ability to export fixed carbon
453 and reductant from the chloroplast. In *t3ko2* exposed to LL (after growth in LL), growth was slow
454 (**Fig. 2E**) and the PQ pool (**Fig. 4C**) was more reduced than in WT cells, while there was little loss
455 of PSII or PSI activities (**Fig. 4A, B, E, F**). These results suggest that there is a reduced rate of
456 PQH2 oxidation. During ML exposure, the mutant stopped growing, and when placed in HL
457 experienced severe bleaching (**Fig. 2F**). The highly reduced PQ pool and PSI reaction center in
458 ML-acclimated *t3ko2* cells (**Fig. 4C, E**, respectively) reflects hyper reduction of PET and the
459 generation of 'over-flow' electrons. The phenotypes of the *t3ko2* cells, including an elevated 1-qL
460 (**Fig. 4C-D**), slower oxidation rate of PSI in ML-acclimated cells (**Fig. 4F**), accumulation of
461 storage carbon (**Fig. 3A-D**), an increase in intracellular accumulation of triose-P and 3-PGA (**Fig.
462 3E**), light dependent damage to the photosynthetic apparatus (**Fig. 4B**) and elevated
463 production/accumulation of ROS (**Fig. 5A, B**), especially in the chloroplast (**Fig. 6B**), indicates a
464 block on the acceptor side of PSI, which reflects the function of CreTPT3 and its central role in
465 fixed carbon export from the chloroplast and for fueling central metabolism.

466 The malate-OAA shuttle represents another route that, under high redox stress, might have
467 partially compensated for the loss of the CreTPT3 by transporting reductant from the chloroplast
468 (schematic in **Fig. 7**). Intriguingly, malate levels in *t3ko2* were 4-fold lower than in WT cells (**Fig.**
469 **3E**, **G**). Moreover, expression of the plastid localized malate dehydrogenases (Cre*MDH1* and
470 Cre*MDH5*) was 3-fold to 5-fold lower in the mutant than in WT cells following a transition from
471 LL to ML (**Supplementary Fig. 10E-F**), indicating that the malate-OAA shuttle is likely unable
472 to compensate for a loss of CreTPT3. Inactivation of CreTPT3 appears to have a negative impact
473 on the malate-OAA shuttle, potentially because of the compromised physiological state of the
474 *t3ko2* mutant. Furthermore, a previous study of metabolic flux analysis during heterotrophic
475 growth of Chlamydomonas showed that the CreTPT shuttle(s) is almost 10-fold more active than
476 the malate-OAA shuttle (Boyle et al., 2017).

477 **TPT deficiency in Chlamydomonas cannot be compensated for by a day/night regime**

478 TPT deficiency in plants can be almost fully compensated for by the starch-mediated night
479 pathways that elicit the breakdown of starch and the export of the breakdown products via the
480 maltose transporter (MEX1) and glucose translocator (GlcT) (Cho et al., 2011). Furthermore, in
481 plants, starch turnover may also be occurring in the light, at the same time as starch is being
482 synthesized (Häusler et al., 1998; Walters et al., 2004). Compared to algae, plant cells appear to
483 display a high plasticity in their capacity to transport fixed carbon between the chloroplast and
484 cytosol. This high degree of plasticity in plants is reflected by the findings: i) most dicots contain
485 a larger number of pPTs (from 5 to 16). For example, Arabidopsis contains 6 pPTs, which includes
486 one TPT, two GPTs, two PPTs and one XPT, whereas Chlamydomonas harbors four PPTs, which
487 include two TPTs, one putative PPT (TPT10 in this study) and one putative GPT/XPT (CGL51 in
488 this study); ii) the plant TPTs play an important role in the export of carbon from the chloroplast
489 during the day. However, XPT has been shown to transport triose-Ps and partially compensate for
490 the loss of TPTs under both ML and HL conditions (Eicks et al., 2002; Hilgers et al., 2018b).
491 Hence, it appears that the paths for fixed carbon export in plants are cooperative, with contributions
492 of transporters that use various sugars, sugar phosphates and triose phosphates.

493 Additionally, the elevated starch content in the *t3ko2* mutant during growth in both LL and ML
494 compared to WT cells suggests that the lesion creates a bottleneck in the export of fixed carbon,
495 which in part becomes stored as starch and lipids (**Fig. 3A-D, Supplementary Fig. 8A**). In this

496 study we found that Chlamydomonas *tpt3* mutants exhibited severe growth retardation and the
497 accumulation of starch and lipid in either continuous light (CL) or when experiencing a day/night
498 regime (**Fig. 2D-G** and **8A**). Furthermore, the light-induced electron transport rate (ETR) through
499 PSII in the *t3ko2* mutant maintained on a diurnal cycle was similar to that of WT cells exposed to
500 actinic light intensities of up to 200 μmol photons m^{-2} s^{-1}, but was approximately 30% lower than
501 that of WT cells at a light intensity of 400 μmol photons m^{-2} s^{-1} (**Fig. 8B**). We also observed that
502 diurnally maintained *t3ko2* cells grew slightly better than when the cells were maintained in CL
503 (**Fig. 8A**), indicating that the loss of CreTPT3 might be partially compensated for by starch
504 turnover during the night (or allow for some repair of cellular damage that might accumulate
505 during the day), but to a lesser extent than in plants. We observed night-time starch degradation in
506 *tpt3* cells, although immediately following the night period a higher level (~5-fold) of undegraded
507 starch remained relative to that of WT cultures (**Fig. 8C**). These data suggest that starch
508 mobilization may partially compensate for a CreTPT3 deficiency in Chlamydomonas.

509 The mechanism by which starch breakdown products are exported from the chloroplast during the
510 night in Chlamydomonas remains largely unknown, although it could involve various transporters
511 including MEX1 (like in plants). Chlamydomonas MEX1 can transport starch break down
512 products in the form of glucose and/or glucose phosphate, but there is no evidence suggesting that
513 it can export maltose since a *mex1* mutant did not accumulate maltose or exhibit growth
514 impairment (Findinier et al., 2017). We speculate that the loss of TPT3 might be partially
515 compensated for by starch turnover in the dark, with degradation products exported via MEX1 or
516 the other pPTs that are highly expressed in the dark and downregulated in the light, such as
517 CreTPT10 and CGL51 (**Supplementary Fig. 9A**, **B**). However, even if hexose-P is exported from
518 the chloroplast, it may not be readily converted to triose-P (see below), which would fuel the TCA
519 cycle and respiration and serve to support anabolic processes.

520 ***t3ko2* experiences oxidative stress**

521 In plants, the export of sugars and other molecules (e.g. redox equivalents/ROS) can serve as
522 signals that coordinate chloroplast and nuclear gene expression during acclimation to HL (Häusler
523 et al., 2014; Zirngibl et al., 2022). We probed the impact of impaired triose-P export in *t3ko2* on
524 ROS production and accumulation in various subcellular compartments following exposure of the
525 cells to ML or HL. In plant cells, H_2O_2 is produced as a side-product of cellular processes including

526 PET, mitochondrial respiration, and substrate level oxidation (Cheeseman; Foyer and Noctor,
527 2016). While ROS stability is generally low, it can accumulate in cells experiencing oxidative
528 stress, with H_2O_2 being the most prevalent species that can function as a redox messenger (Li and
529 Kim, 2022). Moreover, the trafficking of H_2O_2 into or out of different cellular compartments can
530 trigger activation of other retrograde and anterograde signals that may coordinate activities among
531 the compartments, including the nucleus (Exposito-Rodriguez et al., 2017; Mittler et al., 2022;
532 Shapiguzov et al., 2012). Upon exposure to HL, the *t3ko2* mutant accumulated more stromal H_2O_2
533 than WT cells. The cytosolic H_2O_2 levels in the mutant exhibited a similar increase, which may
534 reflect the ability of this metabolite to rapidly diffuse from the chloroplast and into the cytoplasm
535 (**Fig. 6B, C**). Furthermore, it is unlikely that the mitochondrion contributes to an increase in H_2O_2
536 in *t3ko2* since no (or little) increase in accumulation of intramitochondrial H_2O_2 was observed in
537 the mutant in either LL or ML (**Fig. 6D**). An increase in H_2O_2 accumulation in the nucleus of *t3ko2*
538 relative to WT cells was also observed, although the light intensity (HL or LL) did not alter these
539 levels in either WT or the mutant (**Fig. 6E**); a previous report showed that the nuclear H_2O_2 level
540 was not significantly affected in WT Chlamydomonas cells following a HL exposure (Niemeyer
541 et al., 2021), which may reflect both the accumulation of intracellular H_2O_2 and barriers that limit
542 its diffusion. The higher levels of H_2O_2 in the nucleus of *t3ko2* cells may trigger retrograde signals
543 that modulate nuclear gene expressions, which in turn could ameliorate some of the negative
544 effects of ROS and elicit repair of any damage experienced by the photosynthetic apparatus. A
545 similar response may be elicited in WT cells at higher intensity actinic light.

546 It was shown that H_2O_2 can be synthesized in thylakoid membranes as a consequence of the
547 oxidation of plastoquinol (PQH_2), suggesting a positive correlation between the redox state of the
548 PQ pool and the generation of H_2O_2 (Khorobrykh et al., 2015). A similar finding was noted for
549 both *Nicotiana benthamiana* and Chlamydomonas based on the use of hypersensitive H_2O_2 sensors
550 (Exposito-Rodriguez et al., 2017; Niemeyer et al., 2021). These two organisms were shown to
551 accumulate more stromal H_2O_2 in HL, which was dependent on photosynthesis. We observed this
552 positive correlation between PQ pool reduction and the accumulation of H_2O_2 in the *t3ko2* mutant;
553 the PQ pool was more reduced in *t3ko2* relative to the WT cells after exposing the cells to 105 s
554 of HL (**Fig. 4D)**. In parallel, there was a marked increase in stromal H_2O_2 following 2.5 min of HL
555 (**Fig. 6B**). Therefore, hyper-reduction of the PQ pool in the mutant likely results in elevated stromal
556 H_2O_2 accumulation, suggesting that CreTPT3 activity and the export of triose-P from the

557 chloroplast is critical for maintaining low level synthesis/accumulation H_2O_2 and sustaining a high
558 rate of PET in HL; the export of fixed carbon relieves the redox pressure and lessens ROS
559 formation. Additionally, Cre*TPT3* is the most nutrient-deprivation responsive/upregulated of the
560 *PPT* family genes that encode chloroplast localized proteins; it responds strongly to nitrogen,
561 sulfur, and iron deprivation (**Supplementary Fig. 9 D-F**). These findings are in accord with the
562 hypothesis that the ability to traffic fixed carbon from the chloroplast is important for both the
563 distributing carbon to other cellular compartments and relieving oxidative stress in the organelle.

564 **CreTPT3 is critical for maintaining intracellular partitioning of fixed carbon**

565 Why is the phenotype of the Chlamydomonas *tpt3* mutant so severe? Land plants contain the entire
566 glycolytic pathway in both the chloroplast and cytosol while the pathway is partitioned between
567 two compartments in Chlamydomonas; 90% of the upper activities of the pathways (from F6P→
568 3PG) was associated with the plastid while over 95% of the activities of the lower part of the
569 pathway (3PG→Pyruvate) occurred in the cytosol (Klein, 1986; Rochaix et al., 1998). The
570 oxidative pentose phosphate pathway also appears to be in the chloroplast (Klein, 1986). The
571 partitioning of glycolysis between the chloroplast and cytosol is supported by the comparative
572 quantification of the metabolites, with glucose-1-P, fructose-6-P, and fructose-1,6-P2 being
573 exclusively in the chloroplast and 2-phosphoglycerate only in the cytosol (Klöck and Kreuzberg,
574 1991). Recently, it was suggested that the flux of metabolites through hexose-P is negligible in the
575 Chlamydomonas cytosol (Treves et al., 2022), possibly because of the absence of glycolytic
576 reactions that would facilitate its metabolism. Therefore, even if hexose-P is exported from the
577 chloroplast, it would likely not be rapidly metabolized or maintain rapid cell growth. Overall, the
578 results strongly suggest that triose-P exported from the Chlamydomonas chloroplast is likely the
579 major source of fixed carbon transported into the cytoplasm of the cell, facilitating algal growth in
580 the light.

581 Thus, we hypothesize that the export of triose-P would drive the cytosolic segment of glycolysis
582 and downstream metabolic pathways. This hypothesis is supported by the metabolite analysis;
583 specifically, a marked increase of most metabolites associated with the CBBC or the upper-
584 glycolytic/gluconeogenic pathways, and a significant decrease of some metabolites (fumarate and
585 malate) of the TCA cycle upon exposure of the mutant cells to either LL or ML (**Fig. 3E-G,**
586 **Supplementary Fig. 8B, C**). In contrast, elimination of the chloroplast-targeted TPT1 protein of

587 Arabidopsis showed no significant phenotype, although growth was retarded in the TPT/XPT
588 double mutants (Hilgers et al., 2018a). Furthermore, based on Pearson correlation analyses
589 presented in **Supplementary Fig. 11** and **Table. 4**, Cre*TPT3* is co-expressed with many genes
590 involved in respiratory electron transport and the major ATP transporters located on the
591 mitochondria and chloroplast envelope membranes. In addition, transcript levels of some genes
592 involved in starch degradation, glycolysis, the TCA cycle, and malate/OAA shuttle shared a high
593 correlation coefficient with Cre*TPT3*. Together, these data indicate that the export of triose-P from
594 the chloroplast is closely linked to central energy metabolism in Chlamydomonas, starting with
595 the production of triose-P in the chloroplast by the CBBC or starch degradation (chloroplast
596 localized reactions of glycolysis), followed by transport to the cytosol which houses the remaining
597 reactions of glycolysis. The products of glycolysis can be trafficked to the mitochondria where
598 they can be used to drive the TCA cycle, respiratory metabolism and the generation of ATPs
599 (**Supplementary Fig. 11**). Hence, triose-P is the major photoassimilate routed from the chloroplast,
600 suppling substrates for downstream metabolic processes.

601 **Summary**

602 As depicted in **Fig. 7**, we propose that various tiers of regulation are responsible for the
603 physiological responses of the Chlamydomonas *t3ko2* mutant. When *t3ko2* cells are transferred
604 from LL to ML, the triose-P pool and metabolites derived from that pool accumulate because of
605 the reduced capacity of the strain to move triose-P out of the chloroplast where it could be further
606 metabolized. Some compensation may occur through the activity of other transporters, although
607 expression of Cre*TPT2* is especially low during the day (in the light) and the transport of hexose
608 phosphate may not compensate for the loss of CreTPT3 because the cytoplasm does not have (or
609 has little of) the activities of glycolysis that would convert hexose-P to DHAP. The compromised
610 ability to export fixed carbon from the chloroplast also suppresses CBBC activity, causes hyper-
611 reduction of PET and the accumulation of ROS (which would inhibit photosynthetic activity). The
612 highly diminished export of triose-P to the cytoplasm would compromise respiration and
613 downstream biosynthetic processes. Furthermore, hyper-reduction of PET and accumulation of
614 carbon metabolites in the stroma would activate AGPase through allosteric regulation and by the
615 FDX/TRX (ferredoxin/thioredoxin) and NTRC (NADPH-dependent thioredoxin reductase C)
616 redox systems, which would result in starch hyper-accumulation (Ballicora et al., 2000; Lepistö et

617 al., 2013) (**Fig. 7**). Increased ROS accumulation in the mutant chloroplasts and an elevated PET
618 redox state would also elicit the generation of retrograde signals that mediate changes in nuclear
619 gene expression (Wakao and Niyogi, 2021; Suzuki et al., 2012; Shapiguzov et al., 2012),
620 stimulating the synthesis of specific activities that may function to ameliorate the impact of the
621 hyper-reduced state attained in the chloroplast.

622

623 **Material and methods**

624 **Strains and culture conditions**

625 WT Chlamydomonas M10 (CC-4403, isogenic line derived from CC-124) was used as the parental
626 strain for the generation of knockout mutants. Cultures were routinely cultivated in growth
627 chambers (LED-41L2, Percival Scientific, Inc.) at 25°C with continuous shaking on an orbital
628 shaker (VWR OS-500 Shaker) at 120 rpm, in Tris-Acetate-Phosphate (TAP) medium (Harris,
629 2009). Cultures were illuminated with continuous cool white LEDs (LED-41L2, Percival
630 Scientific, Inc.) at low light (LL, 30 μmol photons m^{-2} s^{-1}). Experiments were mostly performed
631 with cells grown in the photoautotrophic TP medium (TAP medium without acetate) and in some
632 cases, in TAP medium, at 25°C, and sparged with air while being shaken at 120 rpm in a growth
633 chamber (LED-41L2, Percival Scientific, Inc.). For growth assays, cultures were inoculated to a
634 density of 0.02 at $OD_{750\ nm}$ (~1×10^5 cells/mL) in TP sparged with air under either LL or moderate
635 light (ML, 250-300 μmol photons m^{-2} s^{-1}) intensities. For spectrophotometric and chlorophyll
636 fluorescence analyses, the experimental design is described in **Supplementary Fig. 5**. Growth
637 assays on solid medium were performed with cultures spotted onto the medium at different
638 dilutions (indicated in the text) and exposed to different light intensities; spot tests for
639 photoautotrophic growth were on TP agar plates and for mixotrophic growth on TAP agar plates.
640 Agar plates were incubated for 7 d under either LL or ML (cool white LED) at 25°C.

641 **Reconstitution into liposomes and transport assays**

642 The procedures for the construction and expression of Cre*TPT2* and Cre*TPT3* in yeast are
643 described in supplemental information (SI). For uptake studies, yeast membranes from cells with
644 and without recombinant His-tagged CreTPT2 or CreTPT3 were enriched and reconstituted into
645 3% (w/v) L-alpha-phosphatidylcholine using a freeze-thaw-sonication procedure (Linka et al.,
646 2008). The reconstituted liposomes were preloaded with 30 mM Pi or phosphorylated metabolites
647 to be tested as potential transport substrates. As a negative control for antiport activity, liposomes
648 were also generated without metabolite preloading. The external counter-exchange substrate was
649 removed via gel filtration on Sephadex G-25M columns (GE Healthcare). Transport assays were
650 initiated by adding 0.25 mM [alpha-^{32}P]-phosphoric acid (6,000 Ci/mmol) to the medium bathing
651 the liposomes and performed as previously described by Linka et al. (2008). Measurements of Km
652 for Pi and competitive inhibition constants (Ki) are described in supplemental information (SI)

653 **Vector construction, transformation, and subcellular localization**

654 The pRam118_VENUS plasmid, which harbors the VENUS gene and the *AphVII* cassette (confers
655 resistance to hygromycin) (Cre01.g045550)(Kaye et al., 2019), was used to express Cre*TPT2*
656 (Cre06.g263850_4532) and Cre*TPT3* (Cre01.g045550_4532). The step-by-step description is in
657 SI. 2-4 µg of the engineered plasmids was linearized and added to 250 µL of a cell suspension of
658 ~3×10^8 cells/mL per reaction. The GeneArt MAX Efficiency Transformation Reagent for algae
659 (Invitrogen) was used for introducing the plasmid into the algal cells by electroporation according
660 to the instructions provided by the manufacturer. Transformants were selected on solid TAP
661 medium containing hygromycin (10 µg/mL; Enzo Life).

662 Drug resistant transformants were visualized for VENUS fluorescence as previously described
663 (Kaye et al., 2019). In brief, transgenic cell lines resistant to hygromycin were screened for
664 VENUS fluorescence using a microplate reader (Infinite M1000; TECAN). Excitation and
665 emission settings were: VENUS, excitation at 515 nm, bandwidth 12 nm and emission at 550 nm,
666 bandwidth 12 nm; chlorophyll excitation was at 440 nm, bandwidth 9 nm and emission was at 680
667 nm, bandwidth 20 nm. The TCS SP8 confocal laser-scanning microscope (Leica) was used to
668 visualize the VENUS fluorescence signal (Kaye et al., 2019).

669 **CRISPR-CAS9 mediated mutagenesis**

670 The Chlamydomonas WT strain CC-124 was used for mutant generation. WT cells were cultured
671 under CL (50 µmol photons m^{-2} s^{-1}) for 2 d to a density of 3-5×10^6 cells/mL. The cells were then
672 concentrated to 2×10^8 cells/mL in 0.5×TAP medium supplemented with 80 mM sucrose. Two
673 single guide RNAs (sgRNA) were designed by CHOPCHOP and synthesized by Integrated DNA
674 Technologies (IDT). The sequences of the generated sgRNAs are: *TPT2*-sg (5′-
675 AUAAGGGCAAGGACAUGUCAGGG -3) for editing exon 8, *TPT3*-sg1 (5′-
676 CGCUGGGCGTCACUUCCCGGCGG -3′) for editing exon 1, and *TPT3*-sg2 (5′-
677 AAGGCCGCUAUCGCCAACGUGGG -3′) for editing of exon 7. The protocol for disruption of
678 Cre*TPT2* and Cre*TPT3* was adapted from (Findinier et al., 2019) and is described in SI.

679 **Complementation of mutants *tpt3* mutants**

680 Mutant strains were transformed with the linearized pRam118_CreTPT3 plasmid. Transformed
681 cells were selected in ML and screened for VENUS fluorescence. Colonies exhibiting VENUS

682 fluorescence and an *AphVII* cassette knock-in at the CAS9 target site were examined for
683 accumulation of the CreTPT3 protein by immunodetection using CreTPT3 antibodies generated
684 by GenScript USA Inc (Piscataway, USA). Immuno-positive colonies were subjected to growth
685 assays using spot tests under ML on either solid TAP or TP medium.

686 **P700 activity measurements**

687 Absorbance spectroscopy [JTS-100 spectrophotometer (SpectroLogiX, TN)] to measure P700
688 activity was performed with dark-adapted liquid cultures (15 µg/mL chlorophyll, in 20 mM
689 HEPES-KOH, pH 7.2, and 10% ficoll) as previously described (Clowez et al., 2021). Actinic light
690 was provided by an orange LED (165 µmol photons m^{-2} s^{-1}) for PSI oxidation, followed by a
691 saturating pulse and dark incubation. 20 µM DCMU and 1 mM hydroxylamine were added to the
692 cell suspension to inhibit linear electron flow (LEF) prior to the measurement. P700 activity was
693 measured by monitoring the absorbance at 705 nm (interference filter 6 nm FWHM was used to
694 create a narrow excitation beam); the absorbance at 740 nm was used to correct for an unspecific
695 contribution to the 705 nm signal.

696 **Chlorophyll fluorescence analysis**

697 Chlorophyll fluorescence used to evaluate photosynthetic electron transport was monitored with a
698 DUAL PAM-100 fluorometer. Cells were acclimated in the dark for 20 min prior to illumination
699 at increasing light intensities (0, 10, 50, 100, 200, 400, 800, 1000, 1200 µmol photons m^{-2} s^{-1}) for
700 2 min at each intensity, or at a constant intensity of 450 µmol photons m^{-2} s^{-1} for 10 min to evaluate
701 1-qL. 1 mM CO_2 ($NaHCO_3$) was added to the reaction mix as an electron acceptor for the CBBC.

702 **ROS measurements and roGFP2 imaging analysis**

703 All strains were grown photoautotrophically in LL for 16-24 h. After dilution with fresh medium,
704 the cultures were transferred to ML and stained with CM-H2DCFDA (Thermo Fisher Scientific)
705 as described in (Kong et al., 2018) for detecting ROS. A step-by-step protocol is given in SI.

706 Constructs containing chloroplast or mitochondria targeting sequences (Crozet et al., 2018) fused
707 to codon-optimized roGFP2 (Vevea et al., 2013) were transformed into WT and mutant strains.
708 Transgenic cell lines were screened for green roGFP2 fluorescence using a microplate reader
709 (Infinite M1000; TECAN); excitation was at 488 nm, bandwidth 9 nm and emission at 525 nm,

710 bandwidth 10 nm. Cells with strong green fluorescence were cultured as shown in **Supplementary**
711 **Fig. 5**. Signals from the transformed lines were visualized using a TCS SP8 confocal laser-
712 scanning microscope (Leica). roGFP2 signals were collected and analyzed as previously described
713 (Vevea et al., 2013). Using the sequential setup of the SP8, roGFP2 signals were collected at the
714 emission wavelength of 510-550 nm immediately following excitation at 405 nm and 488 nm
715 (Vevea et al., 2013). The degree of roGFP2 oxidation was analyzed as the ratio of the emission
716 signals after excitation at 405 nm and 488 nm (Vevea et al., 2013).

717 Plasmids harboring H_2O_2 roGFP2-Tsa2ΔCR sensors (Niemeyer et al., 2021) were obtained from
718 the Chlamydomonas Resource Center (https://www.chlamycollection.org/) (**Supplementary**
719 **Table. 3)**. Cells in which roGFP2-Tsa2ΔCR was targeted to the stroma, cytosol, mitochondrial
720 matrix, or nucleus were initially grown in LL in TAP to exponential growth phase. Cells were then
721 grown in TP in LL for 2 h and shifted either to HL or very low light (10 µmol photons m^{-2} s^{-1}).
722 The oxidation state of the sensor was trapped by the addition of N-Ethylmaleimide (NEM) (Sigma
723 Aldrich) and roGFP2 fluorescence was measured in a plate reader (Infinite M1000; TECAN).
724 Signals were detected using the excitation wavelengths of 410 and 488 nm and the emission
725 wavelength of 514 nm. The degree of sensor oxidation (OxD) was calculated as described in
726 (Niemeyer et al., 2021).

727 **Photosynthesis-Irradiance curve**

728 Photosynthesis-Irradiance curves were measured using a custom Pt-Ag/AgCl polarographic
729 electrode system (ALGI) with a water jacketed (for temperature-control), 1 mL glass reaction
730 chamber. A step-by-step protocol is provided in SI.

731 **Starch and TAG quantification**

732 Cells were grown under LL to mid-exponential phase, diluted to 0.5 µg/mL chl with fresh medium
733 and transferred to and then grown in ML for 24 h or more, as indicated. Starch was measured
734 according to (Klein and Betz, 1978), with slight modification (see SI). Triacylglycerol (TAG)
735 levels were estimated by a fluorometric assay using the dye Nile Red (Thermo Fisher)(Yu et al.,
736 2009). A Nile Red solution (500 µg/mL in acetone) was added to 1 mL of the cell suspensions to
737 a final concentration of 0.5 µg/mL. Samples were then incubated at room temperature for 30 min,

738 and the Nile Red fluorescence emission quantified at 575 nm following excitation at 530 nm using
739 a microplate reader (Infinite M1000; TECAN).

740 **Metabolic analysis**

741 Cells grown in LL were shifted to ML for 45 min or 6 h, as indicated. 45 mL of culture was rapidly
742 quenched in cold saline solution (-2 to -3°C), extracted using cold methanol and then analyzed by
743 LC-MS/MS. Quenching and analysis of metabolites were performed, with modifications,
744 according to (Sake et al., 2020). A step-by-step protocol is described in SI. Metabolite extracts
745 were analyzed using LC-MS/MS, as adapted from (Young et al., 2011). A Phenomenex 150 mm
746 x 2 mm Synergi Hydro-RP column was used on an Agilent 1200 Series HPLC system coupled to
747 an AB Sciex 5500 QTRAP system. LC was performed with a liquid injection volume of 20 µL and
748 a gradient elution with 10 mM tributylamine and 15 mM acetic acid (aqueous phase) in acetonitrile
749 (organic phase) (reagent B) at a constant flow rate of 0.3 mL/min, and a constant temperature of
750 40°C. The gradient profile of the organic phase is as follows: 0% B (0 min), 8% B (10 min), 16%
751 B (15 min), 30% B (16.5 min), 30% B (19 min), 90% B (21.5 min), 90% B (28 min), 0% B (28.5
752 min), and 0% B (35 min). MS analysis was performed in negative mode using a multiple reaction
753 monitoring (MRM) acquisition method. Data acquisition was performed on the ABSciex Analyst
754 1.7 software. Absolute quantification of intracellular metabolites was performed using the
755 quantitation mode on the Analyst software. All chemicals used for metabolite extraction and LC-
756 MS/MS analysis were Optima grade reagents.

757

Acknowledgments:

WH thanks Dr. Masayuki Onishi for advice on the generation of CRISPR mutants and Adrien Burlacot for help with PQ pool measurements.

Funding:

This project has supported by DOE award DE-SC0019417 to ARG. WH was supported solely by a grant from the US Department of Energy, Office of Science, Basic Energy Systems (DE-SC0019417). AK and MCP were supported solely by a grant from the US Department of Energy, Office of Science, Basic Energy Systems (DE-SC0019341 to MP). NB and MM were supported by US Department of Energy, Office of Science, Office of Biological and Environmental Research (BER), (DE-SC0018301 to NB). NL and AP were supported by German Research Foundations (DFG Grant LI1781/2-2). BR was supported by National Science Foundation (Award Number 1645164). RGK and JF were supported by the Department of Plant Biology of the Carnegie Institution for Science. PR was supported by Human Frontier Science Program (HFSP) RGP0046/2018 (to ARG).

Author contributions:

WH, AK, ARG and MP conceptualized the study. WH generated the CRISPR mutants as well as the complemented strain, localized the TPT2 and 3 proteins, analyzed the photosynthetic performances and starch changes over diel cycle. AK performed the experiments of photosynthetic O_2 evolution, extraction of samples for LC-MS/MS, data analysis of LC-MS/MS. AP and NL performed the reconstitution into liposomes and transport activity assays. MM and NB performed LC-MS/MS and analyses of metabolite data. WH and YW analyzed the redox status in the cell. BR performed data mining for transcriptome and the Nile red staining. JF and NF analyzed starch changes upon transition from LL to ML. WH, PR and ARG analyzed PSI and PSII activities. JF and BR constructed roGFP2 associated vectors. WH and ARG wrote the manuscript. ARG, MP, AK, NL, NB, AP, MM and all the other authors helped writing and revising the manuscript.

Competing interests:

All authors declare they have no competing interests.

Data and materials availability:

All data are available in the main text or the supplementary materials.

789 **References**

790 **Ballicora, M.A., Frueauf, J.B., Fu, Y., Schürmann, P., and Preiss, J.** (2000). Activation of the
791 potato tuber ADP-glucose pyrophosphorylase by thioredoxin. J. Biol. Chem. **275**: 1315–
792 1320.

793 **Bhatt, P., Bhandari, G., Turco, R.F., Aminikhoei, Z., Bhatt, K., and Simsek, H.** (2022). Algae
794 in wastewater treatment, mechanism, and application of biomass for production of value-
795 added product. Environ. Pollut. **309**: 119688.

796 **Bockwoldt, M., Heiland, I., and Fischer, K.** (2019). The evolution of the plastid phosphate
797 translocator family. Planta **250**: 245–261.

798 **Boschetti, A. and Schmid, K.** (1998). Energy Supply for ATP-Synthase Deficient Chloroplasts
799 of *Chlamydomonas reinhardii*. Plant Cell Physiol. **39**: 160–168.

800 **Boyle, N.R., Sengupta, N., and Morgan, J.A.** (2017). Metabolic flux analysis of heterotrophic
801 growth in *Chlamydomonas reinhardtii*. PLoS One **12**: e0177292.

802 **Chaux, F., Burlacot, A., Mekhalfi, M., Auroy, P., Blangy, S., Richaud, P., and Peltier, G.**
803 (2017). Flavodiiron proteins promote fast and transient O_2 photoreduction in
804 Chlamydomonas. Plant Physiol. **174**: 1825–1836.

805 **Cheeseman, J.M.** Hydrogen peroxide and plant stress: A challenging relationship.

806 **Cho, M.-H., Lim, H., Shin, D.H., Jeon, J.-S., Bhoo, S.H., Park, Y.-I., and Hahn, T.-R.** (2011).
807 Role of the plastidic glucose translocator in the export of starch degradation products from
808 the chloroplasts in *Arabidopsis thaliana*. New Phytol. **190**: 101–112.

809 **Clowez, S., Renicke, C., Pringle, J.R., and Grossman, A.R.** (2021). Impact of menthol on
810 growth and photosynthetic function of *Breviolum minutum* (Dinoflagellata, Dinophyceae,
811 Symbiodiniaceae) and Interactions with its Aiptasia Host. J. Phycol. **57**: 245–257.

812 **Crozet, P. et al.** (2018). Birth of a photosynthetic chassis: A MoClo toolkit enabling synthetic
813 biology in the microalga *Chlamydomonas reinhardtii*. ACS Synth. Biol. **7**: 2074–2086.

814 **Dorion, S., Ouellet, J.C., and Rivoal, J.** (2021). Glutathione metabolism in plants under stress:
815 beyond reactive oxygen species detoxification. Metabolites **11**: 641.

816 **Eicks, M., Maurino, V., Knappe, S., Flügge, U.-I., and Fischer, K.** (2002). The plastidic pentose
817 phosphate translocator represents a link between the cytosolic and the plastidic pentose
818 phosphate pathways in plants. Plant Physiol. **128**: 512–522.

819 **Exposito-Rodriguez, M., Laissue, P.P., Yvon-Durocher, G., Smirnoff, N., and Mullineaux,**
820 **P.M.** (2017). Photosynthesis-dependent H_2O_2 transfer from chloroplasts to nuclei provides
821 a high-light signalling mechanism. Nat. Commun. **8**: 49.

822 **Findinier, J., Delevoye, C., and Cohen, M.M.** (2019). The dynamin-like protein Fzl promotes
823 thylakoid fusion and resistance to light stress in *Chlamydomonas reinhardtii*. PLoS Genet.
824 **15**: e1008047.

825 **Fischer, K., Kammerer, B., Gutensohn, M., Arbinger, B., Weber, A., Hausler, R.E., and**
826 **Flugge, U.-I.** (1997). A new class of plastidic phosphate translocators: A putative link
827 between primary and secondary metabolism by the phosphoenolpyruvate/phosphate
828 antiporter. Plant Cell **9**: 453.

829 **Fliege, R., Flügge, U.-I., Werdan, K., and Heldt, H.W.** (1978). Specific transport of inorganic
830 phosphate, 3-phosphoglycerate and triosephosphates across the inner membrane of the
831 envelope in spinach chloroplasts. Biochim. Biophys. Acta Bioenerg. **502**: 232–247.

832 **Flügge, U.I., Fischer, K., Gross, A., Sebald, W., Lottspeich, F., and Eckerskorn, C.** (1989).
833 The triose phosphate-3-phosphoglycerate-phosphate translocator from spinach
834 chloroplasts: nucleotide sequence of a full-length cDNA clone and import of the in vitro
835 synthesized precursor protein into chloroplasts. EMBO J. **8**: 39–46.

836 **Flügge, U.I., Häusler, R.E., Ludewig, F., and Fischer, K.** (2003). Functional genomics of
837 phosphate antiport systems of plastids. Physiol. Plant. **118**: 475–482.

838 **Foyer, C.H. and Noctor, G.** (2016). Stress-triggered redox signalling: what's in pROSpect? Plant
839 Cell Environ. **39**: 951–964.

840 **Ge, F., Huang, W., Chen, Z., Zhang, C., Xiong, Q., Bowler, C., Yang, J., Xu, J., and Hu, H.**
841 (2014). Methylcrotonyl-CoA carboxylase regulates triacylglycerol accumulation in the
842 model diatom *Phaeodactylum tricornutum*. Plant Cell **26**: 1681–1697.

843 **Gibson, D.G., Young, L., Chuang, R.-Y., Venter, J.C., Hutchison, C.A., 3rd, and Smith, H.O.**
844 (2009). Enzymatic assembly of DNA molecules up to several hundred kilobases. Nat.
845 Methods **6**: 343–345.

846 **Gietz, R.D. and Schiestl, R.H.** (2007). High-efficiency yeast transformation using the LiAc/SS
847 carrier DNA/PEG method. Nat. Protoc. **2**: 31–34.

848 **González-Ballester, D., Casero, D., Cokus, S., Pellegrini, M., Merchant, S.S., and Grossman,**
849 **A.R.** (2010). RNA-seq analysis of sulfur-deprived Chlamydomonas cells reveals aspects
850 of acclimation critical for cell survival. Plant Cell **22**: 2058–2084.

851 **Haferkamp, I., Deschamps, P., Ast, M., Jeblick, W., Maier, U., Ball, S., and Neuhaus, H.E.**
852 (2006). Molecular and biochemical analysis of periplastidial starch metabolism in the
853 cryptophyte *Guillardia theta*. Eukaryot. Cell **5**: 964–971.

854 **Harris, E.H.** (2009). Chlamydomonas sourcebook: Introduction to Chlamydomonas and its
855 laboratory use 2nd ed. (Academic Press).

856 **Häusler, R.E., Baur, B., Scharte, J., Teichmann, T., Eicks, M., Fischer, K.L., Flügge, U.I.,**
857 **Schubert, S., Weber, A., and Fischer, K.** (2000). Plastidic metabolite transporters and

858 their physiological functions in the inducible crassulacean acid metabolism plant
859 *Mesembryanthemum crystallinum*. Plant J. **24**: 285–296.

860 **Häusler, R.E., Heinrichs, L., Schmitz, J., and Flügge, U.-I.** (2014). How sugars might
861 coordinate chloroplast and nuclear gene expression during acclimation to high light
862 intensities. Mol. Plant **7**: 1121–1137.

863 **Häusler, R.E., Schlieben, N.H., Schulz, B., and Flügge, U.I.** (1998). Compensation of decreased
864 triose phosphate/phosphate translocator activity by accelerated starch turnover and glucose
865 transport in transgenic tobacco. Planta **204**: 366–376.

866 **Hilgers, E.J.A., Schöttler, M.A., Mettler-Altmann, T., Krueger, S., Dörmann, P., Eicks, M.,**
867 **Flügge, U.-I., and Häusler, R.E.** (2018a). The combined loss of triose phosphate and
868 xylulose 5-Phosphate/Phosphate translocators leads to severe growth retardation and
869 impaired photosynthesis in *Arabidopsis thaliana* tpt/xpt double mutants. Front. Plant Sci.
870 **9**: 1331.

871 **Hilgers, E.J.A., Staehr, P., Flügge, U.-I., and Häusler, R.E.** (2018b). The Xylulose 5-
872 Phosphate/Phosphate Translocator Supports Triose Phosphate, but Not
873 Phosphoenolpyruvate Transport Across the Inner Envelope Membrane of Plastids in
874 Arabidopsis thaliana Mutant Plants. Front. Plant Sci. **9**: 1461.

875 **Houille-Vernes, L., Rappaport, F., Wollman, F.-A., Alric, J., and Johnson, X.** (2011). Plastid
876 terminal oxidase 2 (PTOX2) is the major oxidase involved in chlororespiration in
877 Chlamydomonas. Proc. Natl. Acad. Sci. U. S. A. **108**: 20820–20825.

878 **Huang, W., Haferkamp, I., Lepetit, B., Molchanova, M., Hou, S., Jeblick, W., Río Bártulos,**
879 **C., and Kroth, P.G.** (2018). Reduced vacuolar β-1,3-glucan synthesis affects carbohydrate
880 metabolism as well as plastid homeostasis and structure in *Phaeodactylum tricornutum*.
881 Proc. Natl. Acad. Sci. U. S. A. **115**: 4791–4796.

882 **Jack, D.L., Yang, N.M., and Saier, M.H., Jr** (2001). The drug/metabolite transporter superfamily.
883 Eur. J. Biochem. **268**: 3620–3639.

884 **Johnson, X. and Alric, J.** (2013). Central carbon metabolism and electron transport in
885 Chlamydomonas reinhardtii: metabolic constraints for carbon partitioning between oil and
886 starch. Eukaryot. Cell **12**: 776–793.

887 **Jokel, M., Johnson, X., Peltier, G., Aro, E.-M., and Allahverdiyeva, Y.** (2018). Hunting the
888 main player enabling *Chlamydomonas reinhardtii* growth under fluctuating light. Plant J.
889 **94**: 822–835.

890 **Kammerer, B., Fischer, K., Hilpert, B., Schubert, S., Gutensohn, M., Weber, A., and Flügge,**
891 **U.I.** (1998). Molecular characterization of a carbon transporter in plastids from
892 heterotrophic tissues: the glucose 6-phosphate/phosphate antiporter. Plant Cell **10**: 105–
893 117.

894 **Kaye, Y., Huang, W., Clowez, S., Saroussi, S., Idoine, A., Sanz-Luque, E., and Grossman,**
895 **A.R.** (2019). The mitochondrial alternative oxidase from *Chlamydomonas reinhardtii*
896 enables survival in high light. J. Biol. Chem. **294**: 1380–1395.

897 **Khan, M.I., Shin, J.H., and Kim, J.D.** (2018). The promising future of microalgae: current status,
898 challenges, and optimization of a sustainable and renewable industry for biofuels, feed, and
899 other products. Microb. Cell Fact. **17**: 36.

900 **Khorobrykh, S.A., Karonen, M., and Tyystjärvi, E.** (2015). Experimental evidence suggesting
901 that H_2O_2 is produced within the thylakoid membrane in a reaction between plastoquinol
902 and singlet oxygen. FEBS Lett. **589**: 779–786.

903 **Klein, U.** (1986). Compartmentation of glycolysis and of the oxidative pentose-phosphate pathway
904 in *Chlamydomonas reinhardii*. Planta **167**: 81–86.

905 **Klein, U. and Betz, A.** (1978). Fermentative metabolism of hydrogen-evolving *Chlamydomonas*
906 *moewusii*. Plant Physiol. **61**: 953–956.

907 **Klöck, G. and Kreuzberg, K.** (1991). Compartmented metabolite pools in protoplasts from the
908 green alga *Chlamydomonas reinhardtii*: changes after transition from aerobiosis to
909 anaerobiosis in the dark. Biochim. Biophys. Acta **1073**: 410–415.

910 **Knappe, S., Flügge, U.-I., and Fischer, K.** (2003). Analysis of the plastidic phosphate
911 translocator gene family in Arabidopsis and identification of new phosphate translocator-
912 homologous transporters, classified by their putative substrate-binding site. Plant Physiol.
913 **131**: 1178–1190.

914 **Kong, F., Burlacot, A., Liang, Y., Légeret, B., Alseekh, S., Brotman, Y., Fernie, A.R.,**
915 **Krieger-Liszkay, A., Beisson, F., Peltier, G., and Li-Beisson, Y.** (2018). Interorganelle
916 communication: peroxisomal MALATE DEHYDROGENASE2 connects lipid catabolism
917 to photosynthesis through redox coupling in Chlamydomonas. Plant Cell **30**: 1824–1847.

918 **Kramer, D.M., Johnson, G., Kiirats, O., and Edwards, G.E.** (2004). New fluorescence
919 parameters for the determination of QA redox state and excitation energy fluxes.
920 Photosynth. Res. **79**: 209.

921 **Krishnan, A., Kumaraswamy, G.K., Vinyard, D.J., Gu, H., Ananyev, G., Posewitz, M.C., and**
922 **Dismukes, G.C.** (2015). Metabolic and photosynthetic consequences of blocking starch
923 biosynthesis in the green alga *Chlamydomonas reinhardtii sta6* mutant. Plant J. **81**: 947–
924 960.

925 **Lee, S.-K., Eom, J.-S., Voll, L.M., Prasch, C.M., Park, Y.-I., Hahn, T.-R., Ha, S.-H., An, G.,**
926 **and Jeon, J.-S.** (2014). Analysis of a triose phosphate/phosphate translocator-deficient
927 mutant reveals a limited capacity for starch synthesis in rice leaves. Mol. Plant **7**: 1705–
928 1708.

929 **Lee, Y., Nishizawa, T., Takemoto, M., Kumazaki, K., Yamashita, K., Hirata, K., Minoda, A.,**
930 **Nagatoishi, S., Tsumoto, K., Ishitani, R., and Nureki, O.** (2017a). Crystal structure of
931 the triose-phosphate/phosphate translocator in complex with inorganic phosphate.

932 **Lee, Y., Nishizawa, T., Takemoto, M., Kumazaki, K., Yamashita, K., Hirata, K., Minoda, A.,**
933 **Nagatoishi, S., Tsumoto, K., Ishitani, R., and Nureki, O.** (2017b). Structure of the triose-
934 phosphate/phosphate translocator reveals the basis of substrate specificity. Nat Plants **3**:
935 825–832.

936 **Lepistö, A., Pakula, E., Toivola, J., Krieger-Liszkay, A., Vignols, F., and Rintamäki, E.**
937 (2013). Deletion of chloroplast NADPH-dependent thioredoxin reductase results in
938 inability to regulate starch synthesis and causes stunted growth under short-day
939 photoperiods. J. Exp. Bot. **64**: 3843–3854.

940 **Li, M. and Kim, C.** (2022). Chloroplast ROS and stress signaling. Plant Commun **3**: 100264.

941 **Lim, L., Linka, M., Mullin, K.A., Weber, A.P.M., and McFadden, G.I.** (2010). The carbon and
942 energy sources of the non-photosynthetic plastid in the malaria parasite. FEBS Lett. **584**:
943 549–554.

944 **Linka, M., Jamai, A., and Weber, A.P.M.** (2008). Functional characterization of the plastidic
945 phosphate translocator gene family from the thermo-acidophilic red alga *Galdieria*
946 *sulphuraria* reveals specific adaptations of primary carbon partitioning in green plants and
947 red algae. Plant Physiol. **148**: 1487–1496.

948 **Loddenkötter, B., Kammerer, B., Fischer, K., and Flügge, U.I.** (1993). Expression of the
949 functional mature chloroplast triose phosphate translocator in yeast internal membranes
950 and purification of the histidine-tagged protein by a single metal-affinity chromatography
951 step. Proc. Natl. Acad. Sci. U. S. A. **90**: 2155–2159.

952 **Mittler, R., Zandalinas, S.I., Fichman, Y., and Van Breusegem, F.** (2022). Reactive oxygen
953 species signalling in plant stress responses. Nat. Rev. Mol. Cell Biol. **23**: 663–679.

954 **Moog, D., Nozawa, A., Tozawa, Y., and Kamikawa, R.** (2020). Substrate specificity of plastid
955 phosphate transporters in a non-photosynthetic diatom and its implication in evolution of
956 red alga-derived complex plastids. Sci. Rep. **10**: 1167.

957 **Ngan, C.Y. et al.** (2015). Lineage-specific chromatin signatures reveal a regulator of lipid
958 metabolism in microalgae. Nat Plants **1**: 15107.

959 **Niemeyer, J., Scheuring, D., Oestreicher, J., Morgan, B., and Schroda, M.** (2021). Real-time
960 monitoring of subcellular H_2O_2 distribution in *Chlamydomonas reinhardtii*. Plant Cell **33**:
961 2935–2949.

962 **Prabhakar, V. et al.** (2010). Phosphoenolpyruvate provision to plastids is essential for
963 gametophyte and sporophyte development in *Arabidopsis thaliana*. Plant Cell **22**: 2594–
964 2617.

965 **Raghavendra, A.S. and Padmasree, K.** (2003). Beneficial interactions of mitochondrial
966 metabolism with photosynthetic carbon assimilation. Trends Plant Sci. **8**: 546–553.

967 **Riesmeier, J.W., Flügge, U.I., Schulz, B., Heineke, D., Heldt, H.W., Willmitzer, L., and**
968 **Frommer, W.B.** (1993). Antisense repression of the chloroplast triose phosphate
969 translocator affects carbon partitioning in transgenic potato plants. Proc. Natl. Acad. Sci.
970 U. S. A. **90**: 6160–6164.

971 **Rochaix, J.-D., Goldschmidt-Clermont, M., and Merchant, S.** (1998). The molecular biology
972 of chloroplasts and mitochondria in Chlamydomonas J.-D. Rochaix, M. Goldschmidt-
973 Clermont, and S. Merchant, eds (Plenum Publishing Corporation).

974 **Sake, C.L., Newman, D.M., and Boyle, N.R.** (2020). Evaluation of quenching methods for
975 metabolite recovery in photoautotrophic *Synechococcus sp*. PCC 7002. Biotechnol. Prog.
976 **36**: e3015.

977 **Saroussi, S., Sanz-Luque, E., Kim, R.G., and Grossman, A.R.** (2017). Nutrient scavenging and
978 energy management: acclimation responses in nitrogen and sulfur deprived
979 Chlamydomonas. Curr. Opin. Plant Biol. **39**: 114–122.

980 **Schneider, A., Häusler, R.E., Kolukisaoglu, Ü., Kunze, R., Van der Graaff, E., Schwacke, R.,**
981 **Catoni, E., Desimone, M., and Flügge, U.I.** (2002). An Arabidopsis thaliana knock-out
982 mutant of the chloroplast triose phosphate/phosphate translocator is severely compromised
983 only when starch synthesis, but not starch mobilisation is abolished. Plant Journal.

984 **Shapiguzov, A., Vainonen, J.P., Wrzaczek, M., and Kangasjärvi, J.** (2012). ROS-talk - how
985 the apoplast, the chloroplast, and the nucleus get the message through. Front. Plant Sci. **3**:
986 292.

987 **Stocking, C.R. and Larson, S.** (1969). A chloroplast cytoplasmic shuttle and the reduction of
988 extraplastid NAD. Biochem. Biophys. Res. Commun. **37**: 278–282.

989 **Streatfield, S.J., Weber, A., Kinsman, E.A., Hausler, R.E., Li, J., Post-Beittenmiller, D.,**
990 **Kaiser, W.M., Pyke, K.A., Flugge, U.-I., and Chory, J.** (1999). The
991 phosphoenolpyruvate/phosphate translocator is required for phenolic metabolism, palisade
992 cell development, and Plastid-dependent nuclear gene expression. Plant Cell **11**: 1609.

993 **Strenkert, D., Schmollinger, S., Gallaher, S.D., Salomé, P.A., Purvine, S.O., Nicora, C.D.,**
994 **Mettler-Altmann, T., Soubeyrand, E., Weber, A.P.M., Lipton, M.S., Basset, G.J., and**
995 **Merchant, S.S.** (2019). Multiomics resolution of molecular events during a day in the life
996 of Chlamydomonas. Proc. Natl. Acad. Sci. U. S. A. **116**: 2374–2383.

997 **Suzuki, N., Koussevitzky, S., Mittler, R., and Miller, G.** (2012). ROS and redox signalling in
998 the response of plants to abiotic stress. Plant Cell Environ. **35**: 259–270.

999 **Treves, H., Küken, A., Arrivault, S., Ishihara, H., Hoppe, I., Erban, A., Höhne, M., Moraes,**
1000 **T.A., Kopka, J., Szymanski, J., Nikoloski, Z., and Stitt, M.** (2022). Carbon flux through

1001 photosynthesis and central carbon metabolism show distinct patterns between algae, C3
1002 and C4 plants. Nat Plants **8**: 78–91.

1003 **Urzica, E.I., Vieler, A., Hong-Hermesdorf, A., Page, M.D., Casero, D., Gallaher, S.D., Kropat,**
1004 **J., Pellegrini, M., Benning, C., and Merchant, S.S.** (2013). Remodeling of membrane
1005 lipids in iron-starved Chlamydomonas. J. Biol. Chem. **288**: 30246–30258.

1006 **Vevea, J.D., Alessi Wolken, D.M., Swayne, T.C., White, A.B., and Pon, L.A.** (2013).
1007 Ratiometric biosensors that measure mitochondrial redox state and ATP in living yeast
1008 cells. J. Vis. Exp.: 50633.

1009 **Wakao, S. and Niyogi, K.K.** (2021). Chlamydomonas as a model for reactive oxygen species
1010 signaling and thiol redox regulation in the green lineage. Plant Physiol. **187**: 687–698.

1011 **Walters, R.G., Ibrahim, D.G., Horton, P., and Kruger, N.J.** (2004). A mutant of Arabidopsis
1012 lacking the triose-phosphate/phosphate translocator reveals metabolic regulation of starch
1013 breakdown in the light. Plant Physiol. **135**: 891–906.

1014 **Weber, A.P.M., Linka, M., and Bhattacharya, D.** (2006). Single, ancient origin of a plastid
1015 metabolite translocator family in Plantae from an endomembrane-derived ancestor.
1016 Eukaryot. Cell **5**: 609–612.

1017 **Weise, S.E., Liu, T., Childs, K.L., Preiser, A.L., Katulski, H.M., Perrin-Porzondek, C., and**
1018 **Sharkey, T.D.** (2019). Transcriptional regulation of the glucose-6-phosphate/phosphate
1019 translocator 2 is related to carbon exchange across the chloroplast envelope. Front. Plant
1020 Sci. **10**: 827.

1021 **Winder, C.L., Dunn, W.B., Schuler, S., Broadhurst, D., Jarvis, R., Stephens, G.M., and**
1022 **Goodacre, R.** (2008). Global metabolic profiling of Escherichia coli cultures: an
1023 evaluation of methods for quenching and extraction of intracellular metabolites. Anal.
1024 Chem. **80**: 2939–2948.

1025 **Young, J.D., Shastri, A.A., Stephanopoulos, G., and Morgan, J.A.** (2011). Mapping
1026 photoautotrophic metabolism with isotopically nonstationary $^{(13)}$C flux analysis. Metab.
1027 Eng. **13**: 656–665.

1028 **Yu, E.T., Zendejas, F.J., Lane, P.D., Gaucher, S., Simmons, B.A., and Lane, T.W.** (2009).
1029 Triacylglycerol accumulation and profiling in the model diatoms *Thalassiosira*
1030 *pseudonana* and *Phaeodactylum tricornutum* (Baccilariophyceae) during starvation. J.
1031 Appl. Phycol. **21**: 669–681.

1032 **Zhao, Y. et al.** (2018). Malate transported from chloroplast to mitochondrion triggers production
1033 of ROS and PCD in *Arabidopsis thaliana*. Cell Res. **28**: 448–461.

1034 **Zhao, Y., Yu, H., Zhou, J.-M., Smith, S.M., and Li, J.** (2020). Malate circulation: linking
1035 chloroplast metabolism to mitochondrial ROS. Trends Plant Sci. **25**: 446–454.

1036 **Zirngibl, M.-E., Araguirang, G.E., Kitashova, A., Jahnke, K., Rolka, T., Kühn, C., Nägele,**
1037 **T., and Richter, A.S.** (2022). Triose phosphate export from chloroplasts and cellular sugar
1038 content regulate anthocyanin biosynthesis during high light acclimation. Plant Commun:
1039 100423.

1040 **Zones, J.M., Blaby, I.K., Merchant, S.S., and Umen, J.G.** (2015). High-Resolution Profiling of
1041 a Synchronized Diurnal Transcriptome from *Chlamydomonas reinhardtii* Reveals
1042 Continuous Cell and Metabolic Differentiation. Plant Cell **27**: 2743–2769.

1043

Figures and Tables

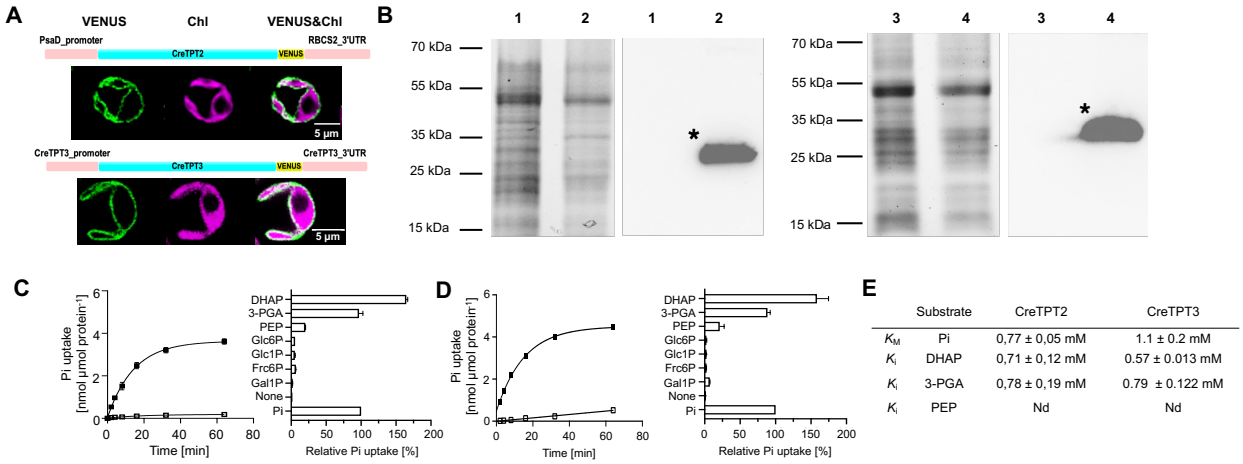

	Substrate	CreTPT2	CreTPT3
K_M	Pi	0,77 ± 0,05 mM	1.1 ± 0.2 mM
K_i	DHAP	0,71 ± 0,12 mM	0.57 ± 0.013 mM
K_i	3-PGA	0,78 ± 0,19 mM	0.79 ± 0.122 mM
K_i	PEP	Nd	Nd

Fig. 1: Subcellular localization of CreTPT2 and 3 and in vitro measurements of transport activities. (**A**) Cellular localization of CreTPT2 (upper) and CreTPT3 (lower). The construct for expression of the CreTPT2/3-VENUS fusion protein is shown above the cell images and described in the **Materials and methods**. VENUS fluorescence, green; Chlorophyll (Chl) autofluorescence, magenta. (Scale bar: 5 µm). (**B**) Expression of Cre*TPT2* (1, 2) and Cre*TPT3* (3, 4) in yeast. **Left in each panel**, SDS-PAGE of proteins from total membranes isolated from yeast cells containing the empty vector (1, 3) or expressing His-CreTPT2 (2) or His-CreTPT3 (4). **Right in each panel**, corresponding immunoblot blot detection of recombinant His-CreTPT2 or His-CreTPT3 protein using anti-His antibodies. The calculated molecular masses of the N-terminal His-tagged proteins of CreTPT2 and CreTPT3 were 39, and 37 kDa. (**C**) **Left**, kinetics of Pi exchange by His-CreTPT2 in lipid vesicles. Uptake of Pi (0.25 mM) into liposomes was measured in the presence (■) or absence (□) of Pi (30 mM) loaded into the vesicles. **Right**, analyses of substrate specificity of His-CreTPT2. (**D**) **Left**, kinetics of Pi exchange by His-CreTPT3 in lipid vesicles. Uptake of Pi (0.25 mM) into liposomes was measured in the presence (■) or absence (□) of Pi (30 mM) loaded into the vesicles. **Right**, analyses of substrate specificity of His-CreTPT3. For the left panels of **C** and **D**, the arithmetic mean (±SD) of three independent experiments (each with three technical replicates) was plotted with respect to the time after initiating the assay. For the right panels of **C** and **D**, liposomes in which His-CreTPT2 and His-CreTPT3, respectively, were incorporated, were preloaded with various substrates (30 mM) and the initial Pi uptake rates (at 0.25 mM external concentration) were determined. Relative velocities were compared to the Pi/Pi homo-exchange, which was set to 100%. The data represents the arithmetic mean (±SD) of three independent experiments (each consisting of three technical replicates). (**E**) Comparison of kinetic constants of His-CreTPT2 and His-CreTPT3. The Michaelis-Menten constant (K_M) for Pi uptake was determined using various external Pi concentrations (0.05-5 mM). The competitive inhibition constant (K_i) of Pi uptake (0.25 mM) was measured with increasing competitor concentrations (0.05-5 mM). Liposomes were preloaded with 30 mM Pi as the counter-exchange substrate. The data represent the arithmetic mean +/- SE of three independent experiments. Nd, no competitive inhibitory constant could be measured under the given experimental conditions. DHAP, dihydroxyacetone phosphate; 3-PGA, 3-phosphoglycerate; PEP, phosphoenolpyruvate; Glc6P, glucose 6-P; Glc1P, glucose 1-P; Fru6P, fructose 6-P; Gal1P, galactose 1-P.

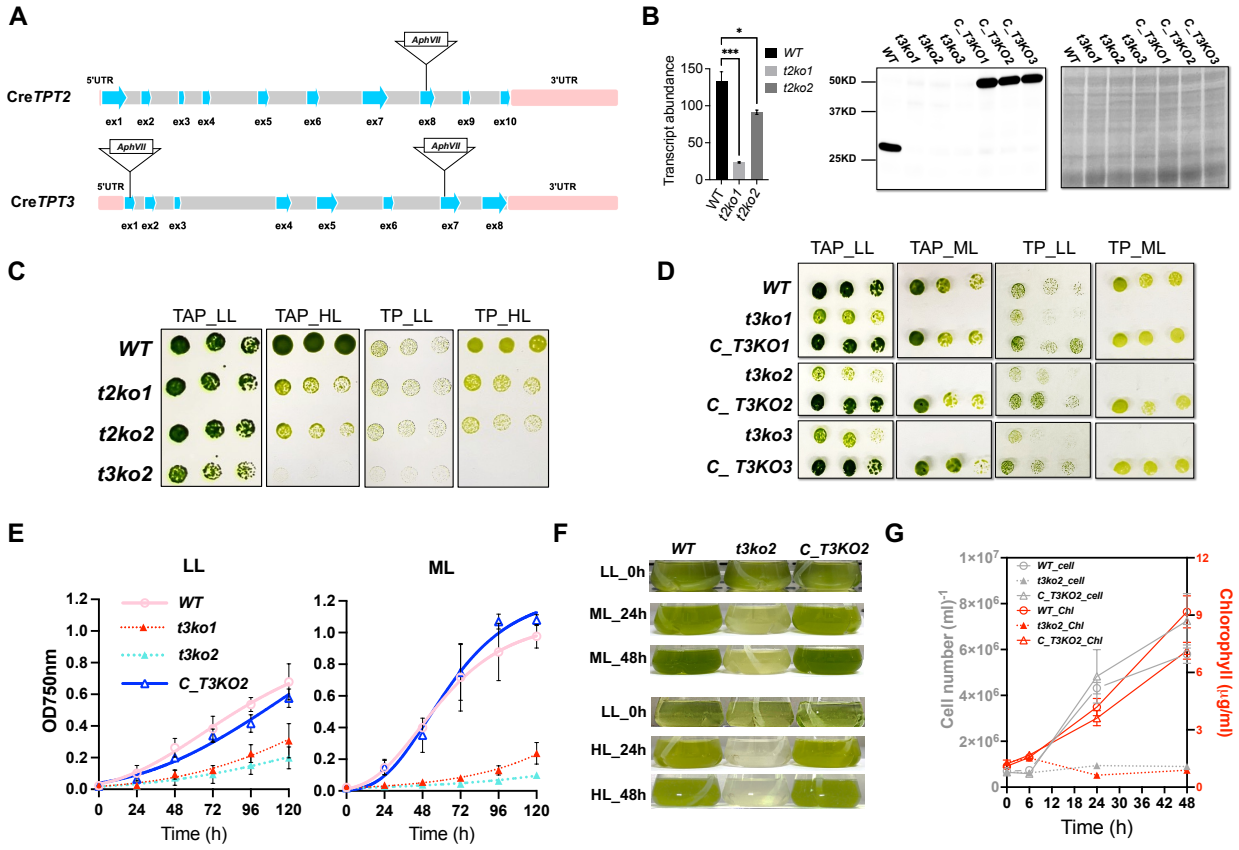

Fig. 2: Growth characterization of *tpt* mutants and complemented strains. (**A**) Molecular map of the Cre*TPT2* (upper) and Cre*TPT3* (lower) genes and the positions of the Cas9 targeted sites. Edited site of Cre*TPT2* is located in exon 8, edited sites of Cre*TPT3* are located in exons 1 and 7; *t3ko1* has the marker gene inserted in exon 1 and *t3ko2* and *t3ko3* have the marker gene inserted in exon 7. (**B**) **Left**, transcript abundances of Cre*TPT2* in WT, *t2ko1* and *t2ko2* strains**. Right**, immunoblot (left panel) of the stained protein profiles (right panel) for wild type (WT), *t3ko1*, *t3ko2*, *t3ko3* and the complemented strains (*C_T3KO1*, *C_T3KO2* and *C_T3KO3*, respectively). (**C**) Growth of WT, *t2ko1*, *t2ko2*, and *t3ko2* at various dilutions (see below) on agar plates incubated under LL and HL for 4 d. (**D**) Growth of WT, *t3ko1*, *t3ko2*, *t3ko3* and the complemented strains (*C_T3KO1*, *C_T3KO2*, and *C_T3KO3*, respectively), at various dilutions (see below) on agar plates incubated under LL and ML for 4 d. (**E**) Growth of the various strains (indicated) in liquid medium under LL (left panel) and ML (right panel). (**F**) Transition of the strains from LL to ML (upper panel) or to HL (lower panel) for the times indicated. (**G**) Cell growth (number) and chlorophyll content of cultures at various times after shifting from LL to ML for up to 48 h. In **C** and **D**, the cells were spotted on agar plates containing TAP or TP medium and maintained under continuous LL, ML or HL conditions. The dilution series used was 1.5, 0.75, 0.375 μg/mL chlorophyll (left to right). For growth in liquid medium, the cells were cultured in TP medium to an initial OD_{750nm} 0.02 in air and under continuous LL before initiating the various growth analyses in LL, ML or HL. Each curve represents the arithmetic mean (±SD) of three independent experiments.

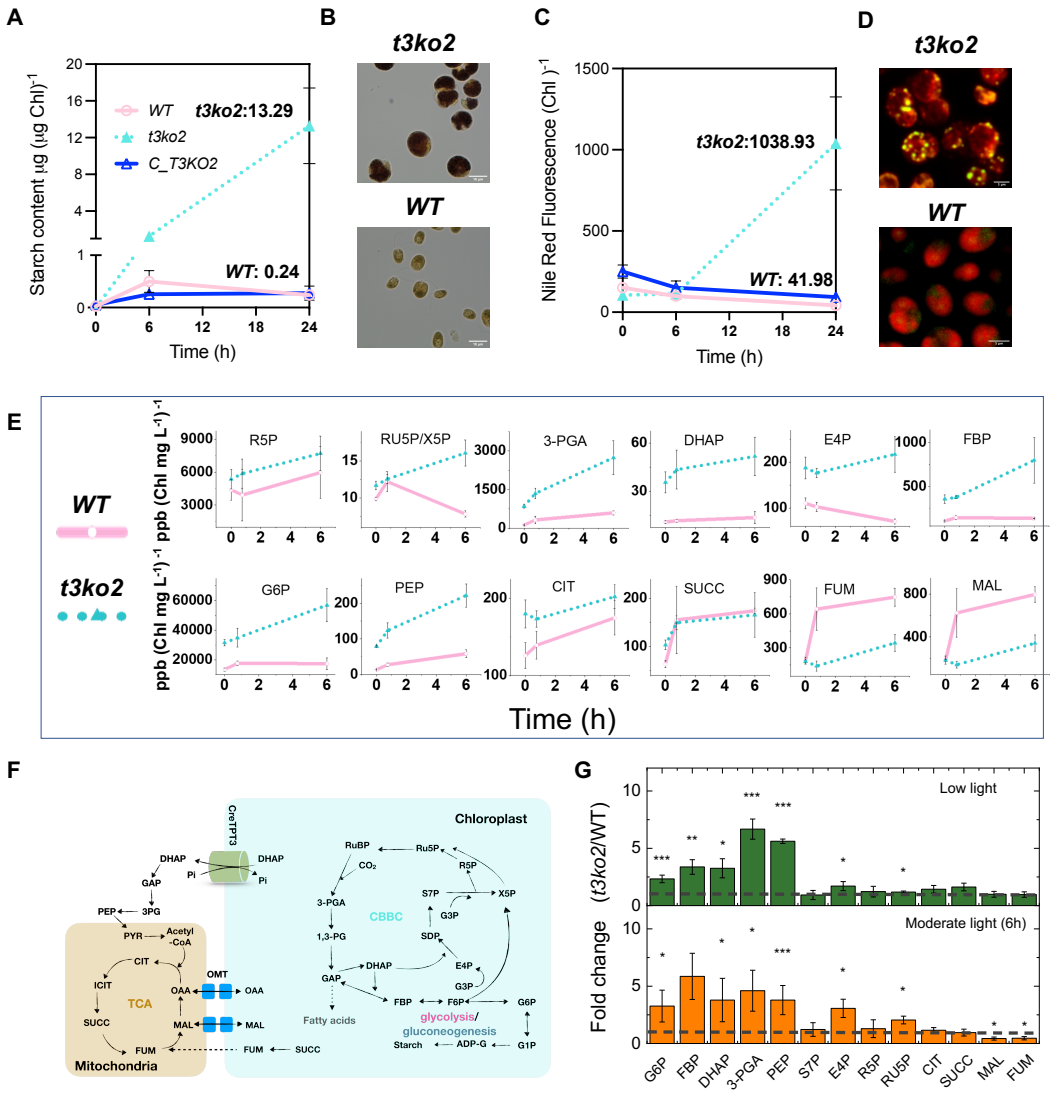

Fig. 3: Changes in storage carbon and metabolite levels in WT and *t3ko2* after transitioning cells from growth in LL to ML. (**A**) Starch content in indicated strains following 0, 6, and 24 h of ML exposure. (**B**) Lugol staining of starch in WT and *t3ko2* after 48 h of ML. (**C**) TAG (TAG: triacylglycerol) content in the indicated strains following 0, 6, and 24 h of ML exposure. (**D**) Nile Red staining of TAG in WT and *t3ko2* following 48 h of ML exposure. (**E**) Time course of metabolite accumulation at 0 h (LL), 45 min and 6 h following ML exposure. (**F**) Select metabolic pathways in Chlamydomonas adapted from (Johnson and Alric, 2013). (**G**) Bar graph representation of fold-change for metabolites shown in (**E**); calculated by dividing the pool size in *t3ko2* by that of WT at the respective light levels. A fold change of 1 (no change) is indicated with a dashed line. Each data point shows the mean and standard error; the data represents three biological replicates for each metabolite. An asterisk indicates statistically significant differences compared to WT (* P<0.05, ** P<0.01, *** P<0.001). Abbreviations: G6P, glucose-6-P; FBP, fructose bisphosphate; DHAP, dihydroxyacetone phosphate; 3-PGA, 3-phosphoglycerate; PEP, phosphoenolpyruvate; PYR, pyruvate; CIT, citrate; SUCC, succinate; FUM, fumarate; MAL, malate; E4P, Erythrose 4-P; R5P, Ribose 5-P; RU5P/X5P, ribulose 5-P/xylulose-5-P; OMT, 2-oxoglutarate/malate transporter.

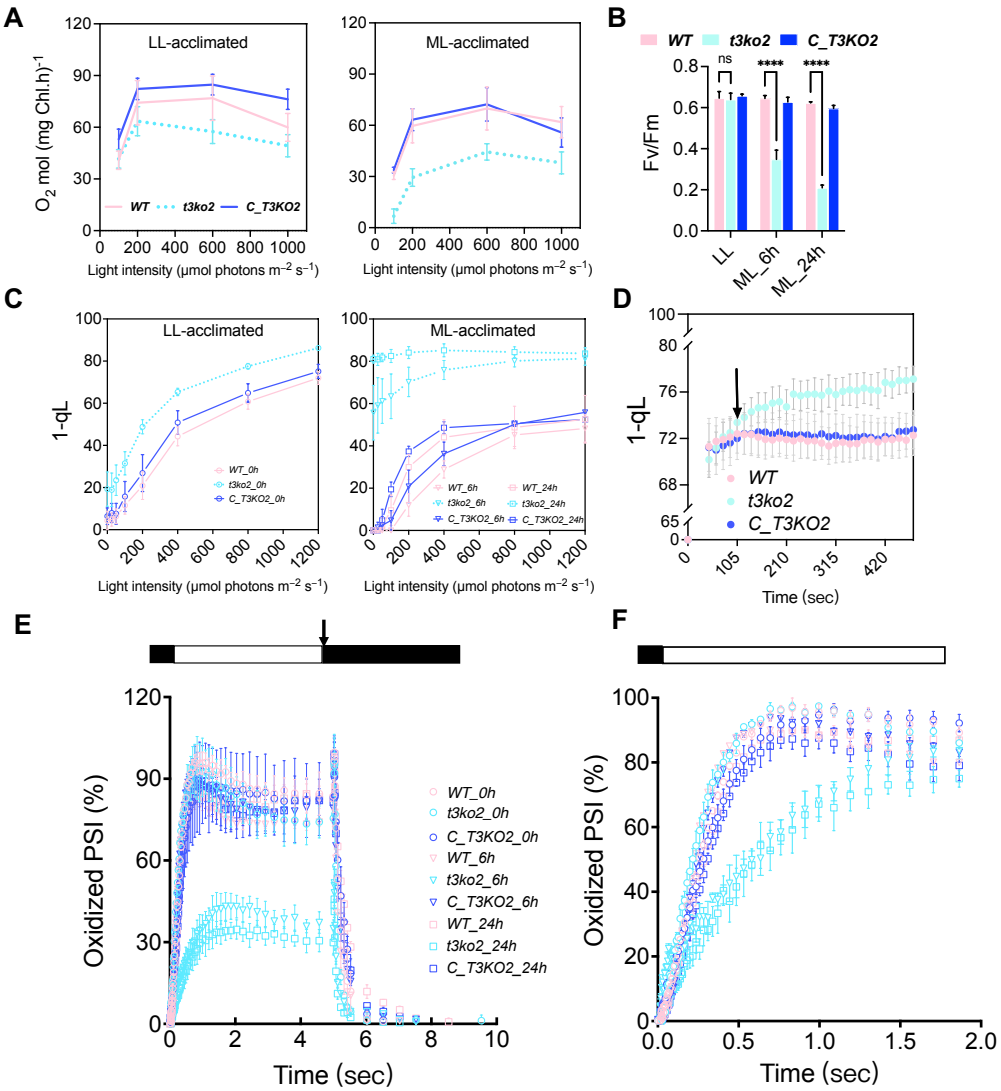

Fig. 4: Photosynthetic activities following a transition from LL to ML or to HL. (**A**) Light intensity curve of O_2 evolution of LL (left) and ML (right)-acclimated cells for the indicated strains. (**B**) Fv/Fm of WT, *t3ko2* and the rescued strain (*C_T3KO2*) following 0 (LL), 6 and 24 h in ML. (**C**) 1-qL values of LL (left panel) and ML (right panel) acclimated cells exposed to increasing actinic light intensities. (**D**) Kinetics of 1-qL of LL-acclimated cells after illumination at HL (400-450 µmol photons m^{-2} s^{-1}) for the times indicated on the x-axis. (**E**) P700 oxidation and reduction kinetics in LL-grown cells and after 6 and 24 h in ML. (**F**) Kinetics of P700 oxidation upon dark-to-light transition. P700 measurements were performed in the presence of DCMU and hydroxylamine, as indicated in the **Materials and methods**. Absorbance differences were monitored at 705 nm during continuous illumination with 150 µmol photons·m^{-2} s^{-1} for 5 sec (white box above), followed by a saturating light pulse at 1,500 µmol photons·m^{-2} s^{-1} (arrow) and a 5 sec dark incubation (black box). For panel **E**, the kinetics was normalized by setting maximum oxidation (after light pulse) of WT to 100% and for panel **F**, by setting maximum oxidation (after light pulse) of individual strain to 100%. The data from all panels represent the arithmetic mean (±SD) of three independent experiments. For panel **B**, the asterisks represent significant differences determined by ANOVA tests., ****$P < 0.0001$.

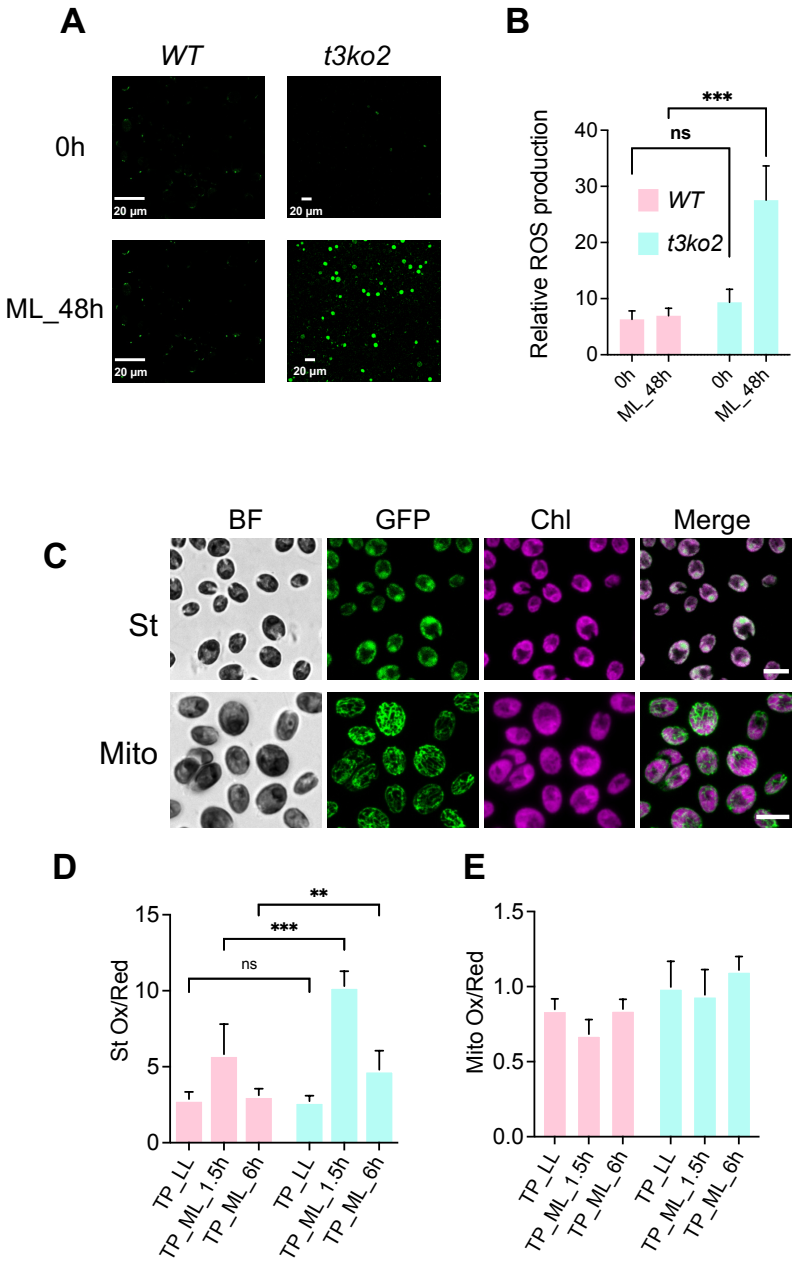

Fig. 5: Measurement of intracellular ROS in *t3ko2* and WT upon transition from LL to ML. (**A**) ROS levels were evaluated by CM-H2DCFDA fluorescence of WT and the *t3ko2* mutant in LL and following exposure to ML for 48 h. (**B**) Quantitation of data in **A**. roGFP2 protein was targeted to the chloroplast stroma (**C**, upper panel) and mitochondrion (**C**, lower panel). Scale bar: 10 µm; BF: bright field; roGFP2 fluorescence: green; Chlorophyll (Chl) autofluorescence: red. (**D-E**) Monitoring redox levels in stroma (**D**) and mitochondrion (**E**) after exposure of WT and the *t3ko2* mutant for 1.5 and 6.0 h of ML. Shown are mean values from three independent experiments, error bars represent standard deviation. For panel **B** and **D**, the asterisks represent significant differences determined by ANOVA tests., **P < 0.005, ***P < 0.001.

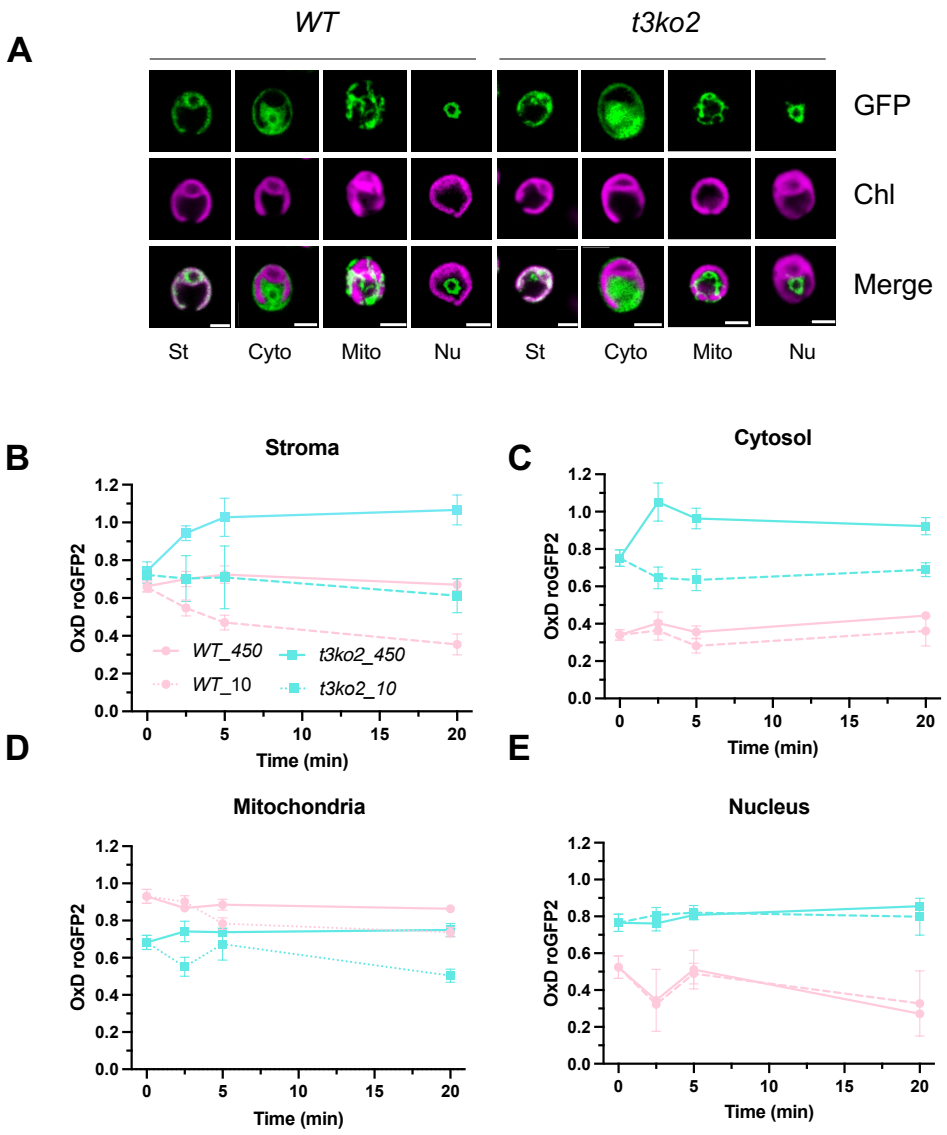

1135

1136 **Fig. 6: Real-time monitoring of H_2O_2 compartmentalized distribution in *t3ko2* and WT upon**
1137 **transition from LL to HL.** (**A**) The hypersensitive H_2O_2 sensor (roGFP2-Tsa2ΔCR) protein was targeted
1138 to the chloroplast stroma (St), cytosol (Cyto), mitochondrion (Mito) and nucleus (Nu). Shown are GFP
1139 fluorescence, chlorophyll autofluorescence (Chl) and the two signals merged (scale bar: 5 µm). WT and
1140 *t3ko2* transformant cells, accumulating roGFP2-Tsa2ΔCR in the stroma (**B**), cytosol (**C**), mitochondrial
1141 matrix (**D**), and nucleus (**E**), were acclimated to LL in TP and then were transferred either to HL (450 µmol
1142 photons m^{-2} s^{-1}, solid line) or to very LL (10 µmol photons m^{-2} s^{-1}, dotted line) for 20 min. The oxidation
1143 state of the sensor was trapped by the addition of NEM and roGFP2 fluorescence was measured in a plate
1144 reader as previously described (Niemeyer et al., 2021). Shown are the mean values from three independent
1145 experiments with the error bars representing the standard deviation.

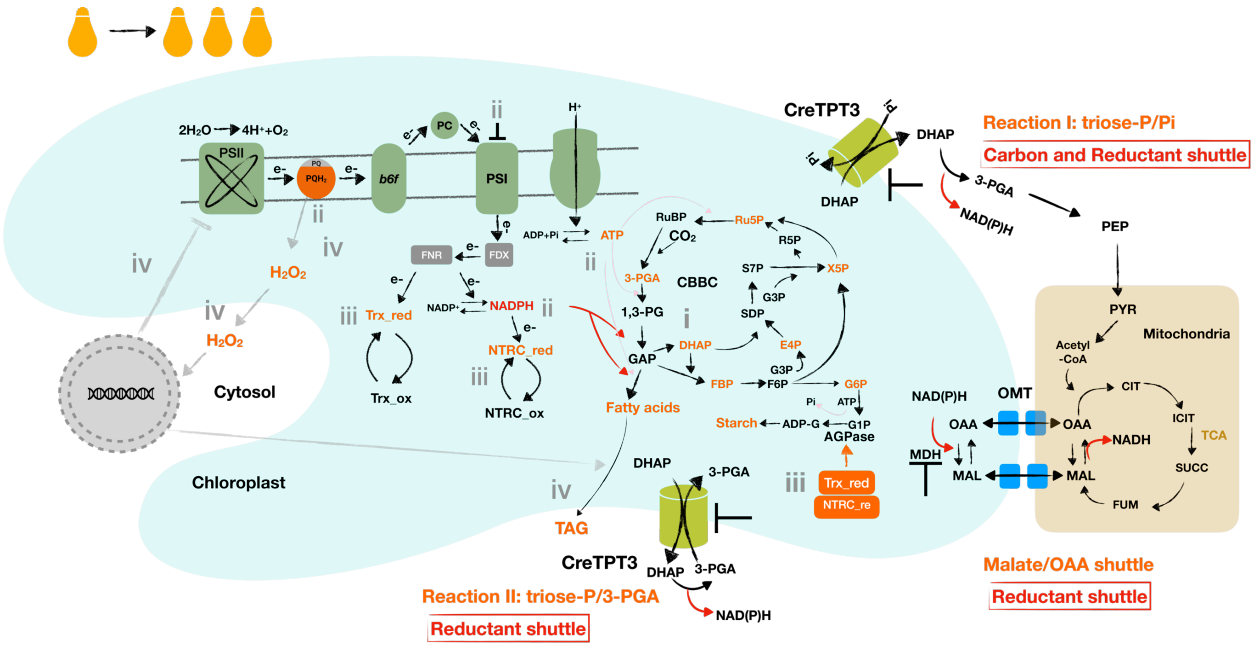

Fig. 7: Impact of eliminating Chlamydomonas TPT3 on the chloroplast metabolic landscape. i. reduced triose-P export leads to accumulation of the sugar-P in CBBC and glycolysis pathways (e.g. triose-P, hexose-P, marked in orange), and an elevated ratio of 3-PGA/Pi (which can allosterically activate AGPase activity) would begin to stimulate the synthesis and accumulation of storage carbon; **ii.** CBBC activity diminishes as a consequence of the hyper-accumulation of the precursors with the fixation of CO_2, leading to elevation of reductant (NADPH) and energy (ATP) within the chloroplast; the elevated NADPH:$NADP^+$ and ATP:ADP ratios, elicit strong feedback on PET causing hyper-reduction of electron carriers (eg: over reduced PQ pool and highly reduced PSI) that slows electron flow across the cytochrome b_6f complex; **iii.** the highly reduced PET system and the elevated NADPH can actively reduce FDX/TRX and the NTRC systems, respectively; reduced TRX and/or NTRC can activate the AGPase (above the activity elicited by an increase in the 3-PGA/Pi ratio), leading to additional starch accumulation; **iv.** hyper-reduction of PET can also lead to stromal ROS accumulation, that can act as a signal that controls expression of chloroplast and nuclear genes; ROS also cause damage to both PSII and I and leads to neutral lipid accumulation as a consequence of activation of diacylglycerol acyltransferases (DGAT) and phospholipid diacylglycerol acyltransferase (PDAT). Many of these metabolic/acclimatory processes both overlap and are interconnected. Under conditions of extended exposure to ML, the damage in Chlamydomonas *tpt3* mutants can accumulate and lead to cell death; cell death occurs rapidly in HL.

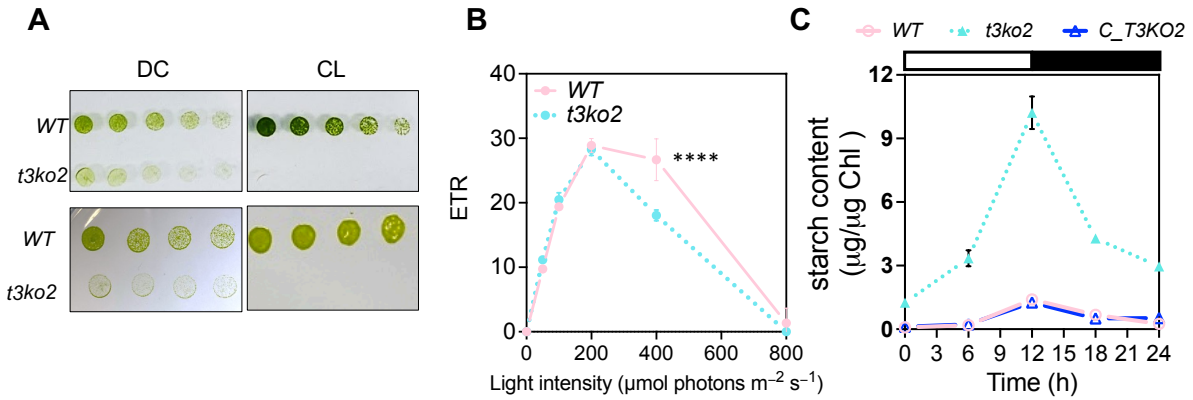

Fig. 8: Effects of deletion of CreTPT3 over diurnal cycle. (**A**) Growth of WT, and *t3ko2* strains on TP agar plates for 4 days either under a diurnal rythym (left panel; light : dark/ 12h : 12h) or continuous light (right panel) at an intensity of 60 µmol photon $m^{-2}s^{-1}$ (upper panel) or HL (lower panel: 450 µmol photon $m^{-2}s^{-1}$). The dilution series are 3, 1.5, 0.75, 0.375 µg/mL chlorophyll. (**B**) Photosynthetic electron transport rate (ETR) of cells grown under a diurnal rythym with the light period at an intensity of 60 µmol photon $m^{-2}s^{-1}$. (**C**) Accumulation of starch during growth under a diurnal rythym at a light intensity of 60 µmol photon $m^{-2}s^{-1}$.

1173 **Supplementary Materials**

1174 **Materials and methods**

1175 **Expression of CreTPT2 and CreTPT3 in yeast**

1176 The DNA sequence encoding the mature CreTPT2 or CreTPT33 protein was codon-optimized for
1177 expression in *Saccharomyces cerevisiae* (GeneART, ThermoFisher Scientific). This coding
1178 sequence was inserted in frame with an N-terminal His tag into the yeast vector pYES-NTa
1179 (ThermoFisher Scientific) using Gibson cloning (NEB). Briefly, pYES-NTa was linearized with
1180 BamHI and the Cre*TPT2* and *TPT3* cDNA amplified with the primer pairs: fwd:5'-
1181 gacgataaggtacctagcGCTGCTGCTGTTCCAGCTG-3' and
1182 rev: 5'- agaattccaccacactgTTAAGCAGCTTCTGGCTTAACATC-3' (for Cre*TPT2*);
1183 fwd: 5' - gacgataaggtacctagcGCTTCTGCTGCTGATGCTC-3'
1184 and rev: 5' - agaattccaccacactgTTAAGCGGCAGCTGGAGAAG-3' (for Cre*TPT3*). This cDNA
1185 was ligated into the linearized pYES-NTa vector, which was then transformed into the yeast strain
1186 INVSc1 (MATa, his3D1, leu2, trp1-289, ura3-52 / MATa, his3D1, leu2, trp1-289, and ura3-52,
1187 Thermo Fisher Scientific) using the lithium-acetate/PEG method (Gietz and Schiestl, 2007).
1188 Transformed yeast cells were selected on synthetic complete medium containing 2% (w/v) glucose
1189 with the uracil auxotrophic marker. Galactose-inducible expression of His-CreTPT2 or CreTPT3
1190 in yeast was performed as described in (Linka et al., 2008). The presence of the His-tagged fusion
1191 protein was verified by standard SDS-PAGE and immunoblot analysis using an anti-His-antibody
1192 conjugated with horseradish peroxidase (Miltenyi Biotech).

1193 **Transport activity assays**

1194 The Km for Pi was determined by measuring the initial velocity at each of six external Pi
1195 concentrations between 0.05 and 5 mM. To obtain competitive inhibition constants (Ki), the uptake
1196 of 0.25 mM Pi into liposomes containing 30 mM Pi was measured over a 4 min period in the
1197 presence of increasing external competitor concentrations (0.05 - 5 mM). Three biological
1198 replicates were performed for all described experiments. GraphPad Prism software version 9.3.0
1199 was used for non-linear regression analyses of the kinetic data.

1200 **Vector construction**

1201 The plasmid of pRam118_VENUS was linearized with HpaI (NEB). Primers: g*TPT2*_pRam118_f,
1202 g*TPT2*_pRam118_r and g*TPT3*_pRam118_f, g*TPT3*_pRam118_r (**Supplementary Table 1**) were
1203 used to amplify Cre*TPT2* and Cre*TPT3* genomic DNAs containing an overlap with the linearized
1204 pRam118_VENUS vector. For generating the plasmids pRam118-CreTPT2&VENUS and
1205 pRam118-CreTPT3&VENUS, genomic DNA of Cre*TPT2* or Cre*TPT3* was assembled with
1206 pRam118_VENUS plasmid using Gibson assembly (Gibson et al., 2009). The plasmid of
1207 pRam118-CreTPT2&VENUS (2-4 µg) linearized with AseI (NEB), was transferred into the
1208 Chlamydomonas M10 strain by electroporation.

1209 A 1,000 bp sequence upstream of Cre*TPT3* and containing the promoter region of the gene was
1210 amplified using the primers TPT3pro1000_f and TPT3pro1000_r (**Supplementary Table 2**). The
1211 3' UTR of Cre*TPT3* was amplified using TPT_3UTR_f and TPT3_3UTR_r (**Supplementary**
1212 **Table 2**). The *PSAD* promoter and the *RBCS2* 3'UTR of pRam118-CreTPT3&VENUS were
1213 replaced by the amplified fragments of the 1,000 bp upstream region and the 3' UTR of Cre*TPT3*,
1214 respectively. This final vector, designated pRam118_CreTPT3, contains the original Cre*TPT3*
1215 promoter (driving expression of Cre*TPT3*), the genomic DNA sequence of Cre*TPT3*, VENUS and
1216 the Cre*TPT3* 3' UTR plus the *AphVII* cassette. To locate CreTPT3 and complement the *tpt3* mutant,
1217 the mutant was transformed by electroporation with a total amount of 2-4 µg (~500 ng/µL) of
1218 pRam118_CreTPT3 that was linearized with AseI.

1219 **CRISPR-Cas9 mediated mutagenesis**

1220 Prior to electroporation, Cas9 (IDT) and sgRNAs were incubated together at 37 °C for 30 min.
1221 Approximately 500 ng PCR product of the *AphVII* cassette, which confers resistance to
1222 hygromycin, was added to the RNP (ribonucleoprotein) mixture. 250 µl aliquots were
1223 electroporated using Super Electroporator NEPA21 type II (NEPA GENE). After 16 h of recovery
1224 in very low light (10-15 µmol photons m^{-2} s^{-1}), cells were plated onto solid TAP medium
1225 containing 10 µg/mL hygromycin. Sense or antisense-oriented knock-ins of *AphVII* were
1226 determined by amplification using primer pairs with one primer annealing to the genomic sequence
1227 and the other to the inserted sequence (**Supplementary Table 2**). The amplified fragments were
1228 sequenced to verify the insertion sites (ELIM BIOPHARM, Hayward, USA).

1229 **ROS measurements and roGFP2 imaging analysis**

1230 Briefly, after various treatment (e.g. 48 h in ML), 10 million Chlamydomonas cells were pelleted
1231 and washed once with 1×PBS. The cells were then resuspended in 1×PBS containing 8 µM CM-
1232 H2DCFDA and incubated at room temperature in the dark for 30 min. Following this incubation,
1233 the cells were washed three times with 1×PBS buffer, the fluorescent signals were either visualized
1234 using TCS SP8 confocal laser-scanning microscope (Leica) or quantified with a microplate reader
1235 (Infinite M1000; TECAN). Excitation and emission settings for the microscope were: 488 nm/510-
1236 530 nm HyD SMD hybrid detector for reactive oxygen species (ROS), and 488 nm/650-700 nm-
1237 HyD SMD hybrid detector for chlorophyll autofluorescence. Excitation and emission settings for
1238 the plate reader were as follows: ROS excitation 488/5 nm and emission 530/12 nm; chlorophyll
1239 excitation 514/5 nm and emission 690/5 nm.

1240 **Starch analysis**

1241 In brief, cells were collected by centrifugation and pigments extracted with methanol. Dried pellets
1242 were resuspended in water and heated at 100ºC to break the cells and release the starch. After
1243 cooling, amyloglucosidase and α-amylase (2.25 U/mL) were used to hydrolyze the starch and the
1244 products of hydrolysis were quantified using a Glucose Colorimetric Detection Kit (Thermo
1245 Fisher).

1246 **Photosynthesis-Irradiance curve**

1247 The YSI 5331A electrodes (Yellow Springs Instruments) were polarized at −0.8 V. The cultures
1248 used for the assays were concentrated to 2.5-5 µg mL^{-1} chlorophyll, supplemented with 15 µL of
1249 0.5 M sodium bicarbonate in water and then purged with 1% CO_2/99% He. Using a gas tight
1250 syringe, the sample was transferred into the reaction chamber that was also purged with 1% CO_2/99%
1251 He. The rate of change in O_2 levels was measured sequentially at the light intensities 100, 200,
1252 600, 1000 µmol photons m^{-2} s^{-1} (photosynthetic active radiation, PAR); each intensity was
1253 maintained for 3-5 min followed by a 3-min intervening dark period, and then the light level was
1254 raised to the next higher intensity (stepped change) until the full range of intensities was tested. At
1255 1,000 µmol photons m^{-2} s^{-1}, the light was held for 10 min followed by an 8-min dark period. Before
1256 the measurement of each experimental series, the electrodes were calibrated with air (~21% O_2)
1257 and 1% CO_2/99% He mixture (0% O_2). The initial slope of the response was used to determine the
1258 O_2 evolution rate.
1259

1260 **Extraction of samples for LC-MS/MS**

1261 The quenching solution, filtered saline (9 g/L NaCl), was prechilled to 4ºC in a refrigerator. 30
1262 mL of the quenching solution was transferred to a 50 mL conical tube kept in an ice bath mixed
1263 with salt to depress the temperature to between -3 ºC and -1 ºC. 15 mL of the culture was rapidly
1264 plunged into the 30 mL of the quenching solution and the samples were centrifuged at 4,000 rpm
1265 for 10 min at 4 ºC. Cell pellets were washed with fresh prechilled saline solution and centrifuged
1266 again at 4,000 rpm for 10 min in a 2 mL centrifuge tube. For each replicate, 45 mL of the culture
1267 was sampled and the cell pellets were pooled. Washed pellets were frozen at -80 ºC until extraction.
1268 Metabolite extraction and further analysis were modified from (Young et al., 2011). To each cell
1269 pellet, 500 µL methanol was added along with the internal standards ribitol and PIPES to a final
1270 concentration of 2 µM each. Samples were then vortexed for 30 sec, frozen in liquid nitrogen as
1271 described in (Winder et al., 2008), and allowed to thaw at 0 °C. This vortex-freeze-thaw cycle was
1272 repeated twice more before the samples were centrifuged at 10,000 x g at 1 °C for 5 min. The
1273 supernatant was collected, and the remaining pellets were extracted twice more with 500 µL of a
1274 50:50 mixture of methanol and water, with 3 vortex-freeze-thaw cycles done for each extraction.
1275 Supernatants from each extraction procedure were pooled and dried on a Thermo Fisher SpeedVac
1276 Concentrator. Dried extracts were then resuspended in 500 µL water and cleaned to remove any
1277 residual large cell debris by filtration, first through a 0.22 µm pore size Spin-X centrifugal tube
1278 filter, followed by 10 K molecular mass cutoff filters, followed finally by 3 K molecular mass
1279 cutoff filters. After each filtration step, filters were rinsed with 50 µL water, which was added to
1280 the total sample volume for subsequent steps. Filtered extracts were dried again and resuspended
1281 in 200 µL water for LC-MS/MS analysis.

1282 **Protein extraction and immunoblot analysis**

1283 Affinity-purified polyclonal antibodies to CreTPT3 were custom-made by GenScript. The antigen
1284 sequence used for antibody generation was KSWSFGRPVTKQEF. Chlamydomonas cells were

1285 grown in liquid cultures to 2–5 x10^6 cells ml^{-1} and collected by centrifugation (1459 x g, 5 min).
1286 Cells were resuspended in resuspension buffer [(5 mM HEPES, pH 7.5, KOH), 10 mM EDTA (pH
1287 7.5, NaOH), 1x protease inhibitor "complete EDTA-free" (Roche)]. For the disruption of cells,
1288 bead-beating was performed using a mini beadbeater (Biospec) in two cycles of 30 sec min^{-1}, with
1289 a 1 min period of cooling on ice between cycles. Disrupted cells were centrifuged at 4 °C, 30 min,
1290 14000 x g in a microfuge. The supernatant was removed, the pellet was resuspended in sample
1291 buffer (resuspension buffer supplemented with 100 mM Na_2CO_3, 100 mM DTT, 2% WT/vol SDS,
1292 and 12% WT /vol sucrose).

1293 SDS-PAGE was performed using a 12% polyacrylamide gel (Bio-Rad), with the electrophoresis
1294 for 90 min at 120 V. The proteins within the gel were transferred onto a PVDF membrane (Bio-
1295 Rad) using Trans-Blot Turbo (Bio-Rad). The detection was performed using Clarity Max Western
1296 ECL Substrate (Bio-Rad).

1297 **RT-qPCR**

1298 RT-qPCR, was performed as described previously (Kaye et al., 2019). Briefly, total RNA was
1299 isolated using the RNeasy Plant Mini Kit (Qiagen) and treated with DNase I (Qiagen). First-strand
1300 cDNA was generated by reverse transcription of 0.5 µg total RNA using the iScript cDNA
1301 Synthesis Kit (Bio-Rad). Real-time PCR using the Roche Light Cycler 480 was performed with
1302 the SensiMix NO-Rox SYBR Green I Kit as described by the manufacturer (Bioline). Oligos used
1303 in this research for analyzing the expression levels of Cre*TPT10/TPT2/TPT3/CGL51* are listed in
1304 **Supplemental Table 1**.

1305 **Analysis of transcript levels in response to different conditions**

1306 In order to analyze the transcript level of Cre*TPT* genes under different conditions, we obtained
1307 RNAseq data published previously in which cells experienced a diurnal cycle, nitrogen starvation,
1308 sulfur starvation and Fe^{2+} starvation (Strenkert et al., 2019; Zones et al., 2015; Ngan et al., 2015;
1309 González-Ballester et al., 2010; Urzica et al., 2013). The log2 fold change of each gene was
1310 calculated based on the ratio of transcript abundance at different time point over transcript level at
1311 time point 0 h. The fold change was visualized by a heatmap and the color bar is the scale of log2
1312 (fold-change).

1313 **Correlation analysis based on Cre*TPT3* transcription abundance under different conditions**

1314 The Z score of each gene was calculated as follows: the mean transcript level of each gene from
1315 all of the conditions was subtracted from each gene's transcript level. This difference was divided
1316 by the standard deviation of each gene's transcript level under all conditions to get Z score numeric
1317 values. The whole Z score matrix for every gene under all conditions was used to calculate the
1318 Pearson correlation matrix by using python. Dataframe.corr() function. The genes highly
1319 correlated with TPT3 were selected if their correlation value is higher than 0.75. The Pearson
1320 correlation value of TPT3-highly-correlated genes were plotted based on their KEGG pathway.

1321 **In vivo polymeric carbohydrate staining**

1322 Lugol's iodine (aqueous solution of 1.8% iodine and 3.0% potassium iodide) was used to stain in
1323 vivo polymeric carbohydrate. Briefly, 0.5 mL of the cell culture was pelleted, resuspended in 10
1324 µL of Lugol's iodine and visualized under a bright-field microscope. Lugol's iodine selectively
1325 binds to alpha-1,4 glucans and stains it blue-black.

1326

Cre ID	Name from V6.1 / (name used in this study)	Previous name	Prediction	CS Position
Cre08.g379350_4532	**TPT10 / (TPT10)**	**TPT1**	**cTP**	**CS pos: 61-62. TCL-AV. Pr: 0.3994**
Cre06.g263850_4532	**N / (TPT2)**	**PPT2; TPT2; TPT20**	**cTP**	**CS pos: 70-71. VCQ-AA. Pr: 0.5253**
Cre01.g045550_4532	**TPT3 / (TPT3)**	**TPT3**	**cTP**	**CS pos: 60-61. VTK-AS. Pr: 0.4178**
Cre02.g106200_4532	N	TPT4; TPT5	OTHER	
Cre02.g112900_4532	N	TPT5; TPT6	OTHER	
Cre02.g144300_4532	N	TPT6; TPT7	OTHER	
Cre03.g162000_4532	N	TPT7; TPT8	OTHER	
Cre03.g184850_4532	N	TPT8; TPT9	OTHER	
Cre04.g227450_4532	N	TPT9	OTHER	
Cre07.g330850_4532	N	TPT10; TPT11	OTHER	
Cre08.g363600_4532	N	TPT11; TPT12	OTHER	
Cre09.g408400_4532	N	TPT12; TPT13	OTHER	
Cre09.g413700_4532	N	TPT13; TPT14	OTHER	
Cre08.g382350_4532	EZY14	TPT14; TPT16; EZY14	OTHER	
Cre09.g415900_4532	MOT20	TPT15	OTHER	
Cre10.g452750_4532	N	TPT16; TPT18	OTHER	
Cre11.g479950_4532	CGL7	TPT17	OTHER	
Cre12.g490050_4532	N	TPT18; TPT19; GMT1	OTHER	
Cre12.g490100_4532	TPT2	TPT19;GMT2	OTHER	
Cre12.g501000_4532	N	TPT20; TPT22; PPT1	OTHER	
Cre15.g641266_4532	N	TPT22; TPT23	OTHER	
Cre15.g642950_4532	N	TPT23; TPT24	OTHER	
Cre15.g643385_4532	N	TPT24; TPT26	OTHER	
Cre16.g663800_4532	**CGL51 / (CGL51)**	**TPT25**	**cTP**	**CS pos: 70-71. IVA-SS. Pr: 0.4817**
Cre16.g666250_4532	N	TPT26; TPT27	OTHER	
Cre17.g702700_4532	N	TPT27; TPT28	OTHER	
Cre17.g703250_4532	SLC35D	TPT28; TPT29	OTHER	
Cre17.g710850_4532	N	TPT29; TPT4	OTHER	
Cre11.g467754_4532	N	UAA6	OTHER	
Cre14.g622700_4532	N	N	OTHER	
Cre18.g748947_4532	N	N	OTHER	
Cre09.g408428_4532	N	N	OTHER	

Supplementary Table 1: Members of the triose phosphate transporter family in *Chlamydomonas reinhardtii* and their predicted subcellular localization based on TargetP-2.0. cTP, chloroplast transit peptide; CS position, cleavage site of transit peptides; N: genes without names in the genome. Cre IDs are from v6.1 genome.

oligo name	sequence
gTPT2_pRam118_f	tactcacaacaagcccagttatggcgtctctgctgggc
gTPT2_pRam118_r	gagccacccagatctccgttggcggcctccggcttgac
gTPT3_pRam118_f	tactcacaacaagcccagttATGGCTTCGCTCGCTCAGCGCGTGAGC
gTPT3_pRam118_r	gagccacccagatctccgttGGCCGCGGCCGGCGACGC
TPT3pro1000_f	gccttttgctcacatgtggcggccgccgccatgctggccaacag
TPT3pro1000_r	taccaatccacaaatgtgggctagcccatgtgaaggcgttgacc
TPT3_3UTR_f	gatgacgacaagtaaagatctTAAGGCGGGCAGCGGC
TPT3_3UTR_r	GCGCAAGAAAGAAGCTTGATATCCCCCTTATAATGTTTACAAGTGGTGCG
hygro_crispr_f2	GGAACTGGCGCAGTTCCTCTG
hygro_crispr_re2	GGCTCGCGTAGGAATCATCCG
TPT2_gRNA1_F	TGGGACGGGAGGTGGAGAGC
TPT3_gRNA1_F	GCTCGGTTGAGCGCACCC
TPT3_gRNA1_R	CAAGGGTCTGGCGAGCACG
TPT3_gRNA2_F	ACCTCCCCATCGCCACGAT
TPT3_gRNA2_R	AGGGGTAAGGACAGCGGTG
Qrt_TPT10_f	CCTGTACCAGCAGGTGTCGTAC
Qrt_TPT10_r	CCAGCGCGTTCTGGAGTGACA
Qrt_TPT2_f	ATGGCGTCTCTGCTGGGC
Qrt_TPT2_r	CTGCTCGCCCATTCTCCTC
Qrt_TPT3_f	GCAAAGCTGGCGCCTACTG
Qrt_TPT3_r	TAGACCAGGCCGACCACCAC
Qrt_CGL51_f	CTGGTTCATCGGGACATGGC
Qrt_CGL51_r	TGGCTGAAGCTGACCACT
Qrt_MDH1_f	GGCTCTGCTGCTGAAGATGAAC
Qrt_MDH1_r	CGGTGTAGCCAGTAACCTTCAC
Qrt_MDH5_f	GGCCCTGAACATGAAGCAGC
Qrt_MDH5_r	GGCGGAAGACTCCATAGGCC
TPT2_qrtko_f	GCGTCGCTGATCGCCTTC
TPT2_qrt_ko_r	CCCTTGCCCTTGTATTTCCG

Supplementary Table 2: Oligonucleotide list.

ID	Construct	Restriction enzyme for transformation	Localization
pMBS472	PSADpro::aadA::PSAD-T:::: ARpro::roGFP2-Tsa2ΔCR::MStop::RPL23-T	ECoRV/AfeI	cytosol
pMBS652	PSADpro::aadA::PSAD-T:::: ARpro::CDJ1::roGFP2-Tsa2ΔCR::MStop::RPL23-T	ECoRV/AfeI	stroma
pMBS657	PSADpro::aadA::PSAD-T:::: ARpro::roGFP2-Tsa2ΔCR::SV40::RPL23-T	ECoRV/AfeI	nucleus
pMBS655	PSADpro::aadA::PSAD-T:::: ARpro::HSP70C::roGFP2-Tsa2ΔCR::MStop::RPL2	ECoRV	mitochondrion

Supplementary Table 3: Plasmids of H_2O_2 roGFP2-Tsa2ΔCR sensors (Niemeyer et al., 2021)**.**

Name	Cre number	Gene function	Correlation coefficient	Localization
TPT3	Cre01.g045550	Triose phosphate/phosphate translocator 2	1	chloroplast
AMY	Cre08.g362450	Alpha-amylase	0.881792677	chloroplast
SP	Cre07.g336950	Starch phosphorylase	0.861504451	chloroplast
ISA3	Cre03.g207713	Isoamylase, starch debranching enzyme	0.790501386	chloroplast
PGI1	Cre03.g175400	Phosphoglucose isomerase	0.808137223	chloroplast
PFK2	Cre12.g553250	Phosphofructokinase	0.805294876	chloroplast
PGM1	Cre06.g272050	Phosphoglycerate mutase	0.838232423	other
IDH2	Cre02.g143250	Isocitrate dehydrogenase, NAD-dependent	0.81622058	other
MDH4	Cre12.g483950	Malate dehydrogenase 4	0.80363604	mitochondrion
PDH1	Cre16.g677026	Pyruvate dehydrogenase E1 beta subunit	0.805186998	mitochondrion
ASAP3	Cre07.g338050	Mitochondrial F1F0 ATP synthase associated protein 3	0.853067434	mitochondrion
MPPB	Cre12.g523850	Mitochondrial processing peptidase beta subunit and Complex III Core I subunit	0.844453019	mitochondrion
NUO5	Cre10.g450400	NADH dehydrogenase (ubiquinone) flavoprotein 2,mitochondrial(respiratory Complex I)	0.781322987	mitochondrion
NUO6	Cre10.g422600	NADH:ubiquinone oxidoreductase 51 kDa subunit,mitochondrial, respiratory Complex I	0.770479958	mitochondrion
COX2a	Cre03.g154350	Mitochondrial cytochrome c oxidase subunit II	0.824639841	mitochondrion
COX2	Cre01.g049500	Mitochondrial cytochrome c oxidase subunit II, protein IIb of split subunit	0.814345856	mitochondrion
COX3	Cre04.g221700	Mitochondrial cytochrome c oxidase subunit III	0.813942712	mitochondrion
COX90	Cre16.g691850	Cytochrome c oxidase subunit Cox90, mitochondrial	0.803959451	mitochondrion
COX10	Cre12.g516350	Mitochondrial cytochrome c oxidase assembly protein	0.770332065	mitochondrion
ATP1a	Cre02.g116750	Mitochondrial F1F0 ATP synthase, alpha subunit	0.850554844	mitochondrion
ATP2	Cre17.g698000	Mitochondrial F1F0 ATP synthase, beta subunit	0.839116637	mitochondrion
ATP3	Cre15.g635850	Mitochondrial F1F0 ATP synthase, gamma subunit	0.790390859	mitochondrion
ATP4	Cre11.g467707	Mitochondrial F1F0 ATP synthase, delta subunit	0.782621502	mitochondrion
ASA7	Cre09.g416150	Mitochondrial F1F0 ATP synthase associated protein 7	0.762529504	mitochondrion
ATP5	Cre16.g680000	Mitochondrial ATP synthase subunit 5	0.75995889	mitochondrion
CYC1	Cre15.g638500	Ubiquinol:cytochrome c oxidoreductase cytochrome c1,mitochondrial	0.78087886	mitochondrion
OMT1	Cre17.g713350	Oxoglutarate:malate antiporter1	0.7724107	chloroplast
MDH1	Cre03.g194850	NAD-dependent malate dehydrogenase	0.770420148	chloroplast
ANT1	Cre09.g386650	ADP/ATP carrier protein, mitochondrial	0.841663755	mitochondrion
AAA1	Cre08.g358526	Plastidic ADP/ATP translocase	0.831658774	chloroplast
ATPva3	Cre04.g220350	Vacuolar ATP synthase subunit A	0.806662753	other
VTC1	Cre12.g510250	Vacuolar Transport Chaperone-like protein	0.753558866	other
PST1	Cre07.g331550	Phosphoserine aminotransferase	0.787494263	chloroplast
CPL12	Cre10.g466500	Glyoxalase	0.787085275	chloroplast
NAGSAD	Cre03.g146187	N-acetyl-gamma-glutamyl-phosphate reductase / NAGSA dehydrogenase/oxidoreductase	0.772201917	chloroplast
NAGK1	Cre01.g015000	Acetylglutamate kinase/L-arginine biosynthesis II (acetyl cycle)	0.771816595	chloroplast
PFGS	Cre08.g364800	Phosphoribosylformylglycinamidine synthase /superpathway of purine nucleotides	0.761886415	chloroplast
PPP2r2	Cre01.g055420	serine/threonine-protein phosphatase 2A regulatory subunit B	0.776264136	chloroplast
CLTC	Cre02.g101400	clathrin heavy chain	0.775380317	other
SLC40a1	Cre06.g251000	solute carrier family 40	0.771233669	secretory pathway

Supplementary Table 4: List of genes with strong correlation to Cre*TPT3*.

A

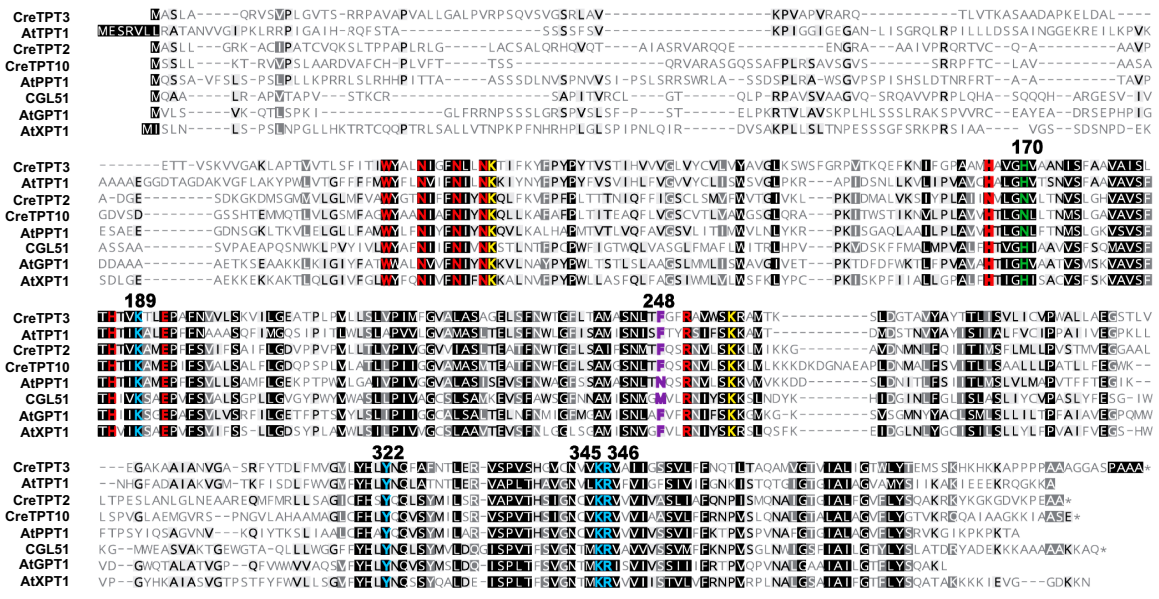

B

p*PT* genes	Similarity (%)	Identity (%)
Cre*TPT3*	57.11	37.3
Cre*TPT2*	48.7	32
Cre*TPT10*	48.4	29.6
CGL51	46.8	29.8

Supplementary Fig. 1: Features of putative plastid phosphate transporter (pPT) in *Arabidopsis thaliana* and *Chlamydomonas reinhardtii*. (**A**) Alignment of sequences of pPTs in Arabidopsis and Chlamydomonas. Plastid putative sugar phosphate transporters from Chlamydomonas are CreTPT10 (Cre08.g379350_4532), CreTPT2 (Cre06.g263850_4532), CreTPT3 (Cre01.g045550_4532), and CGL51 (Cre16.g663800_4532). Sequences from *Arabidopsis thaliana* are AtTPT1 (AT5G46110.1), AtPPT1 (AT5G33320.1), AtGPT1 (AT5G54800.1) and AtXPT1 (AT5G17630.1). Conserved substrate binding pockets are colored red. Phosphate-binding residues are colored blue. The gate capping residues are colored yellow. The positions of residue in green are crucial for the substrate preference of either triose-phosphate or 3-PGA. The purple residues are critical for the specificity of PEP. (**B**) The similarity and identity of the protein sequences between Chlamydomonas pPTs and Arabidopsis TPT1. The similarity and identity were calculated using https://www.bioinformatics.org/sms2/ident_sim.html.

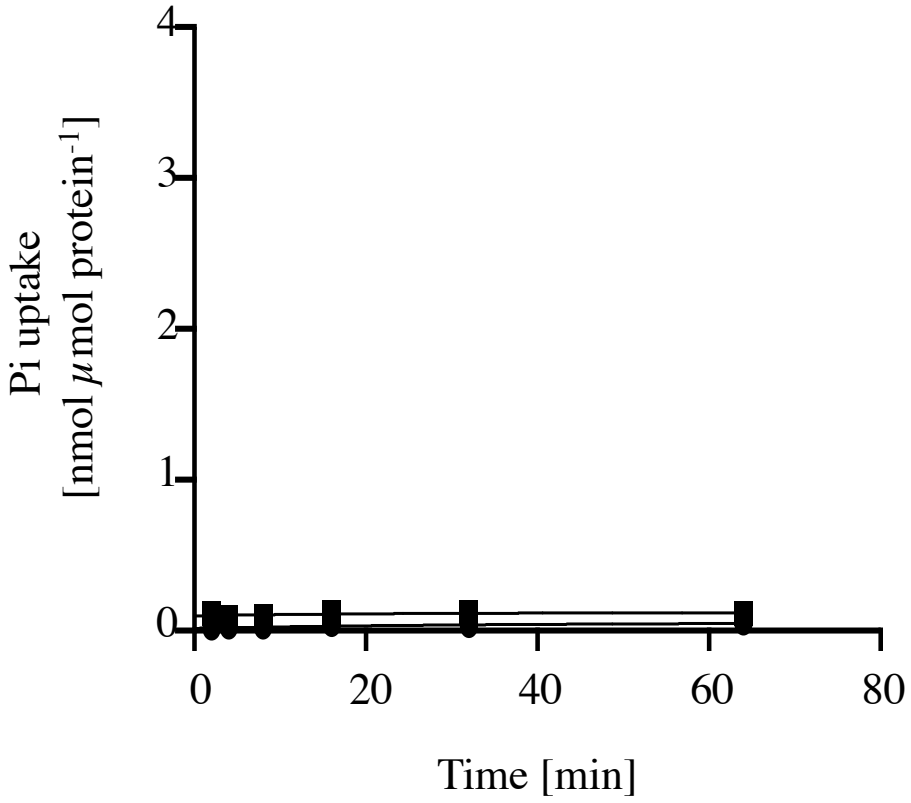

1352

1353 **Supplementary Fig. 2: Background activity of Pi uptake with the endogenous yeast transporters**
1354 **reconstituted in into liposomes.** Time-dependent uptake of Pi (0.25 mM) into reconstituted liposomes
1355 preloaded with 30 mM of Pi (■) or without exchange substrate (●) prepared from yeast cells harboring the
1356 empty vector (pYES-NTa). The arithmetic mean (±SD) of three independent experiments (each with three
1357 technical replicates) was plotted against time. The observed Pi uptake rates of endogenous yeast carriers
1358 reconstituted into liposomes were negligible compared to the rates with His-CreTPT2/3 (20-fold higher,
1359 **Fig. 1C, D**), indicating that this expression system is suitable for functional analysis of recombinant
1360 phosphate transporters.

1361

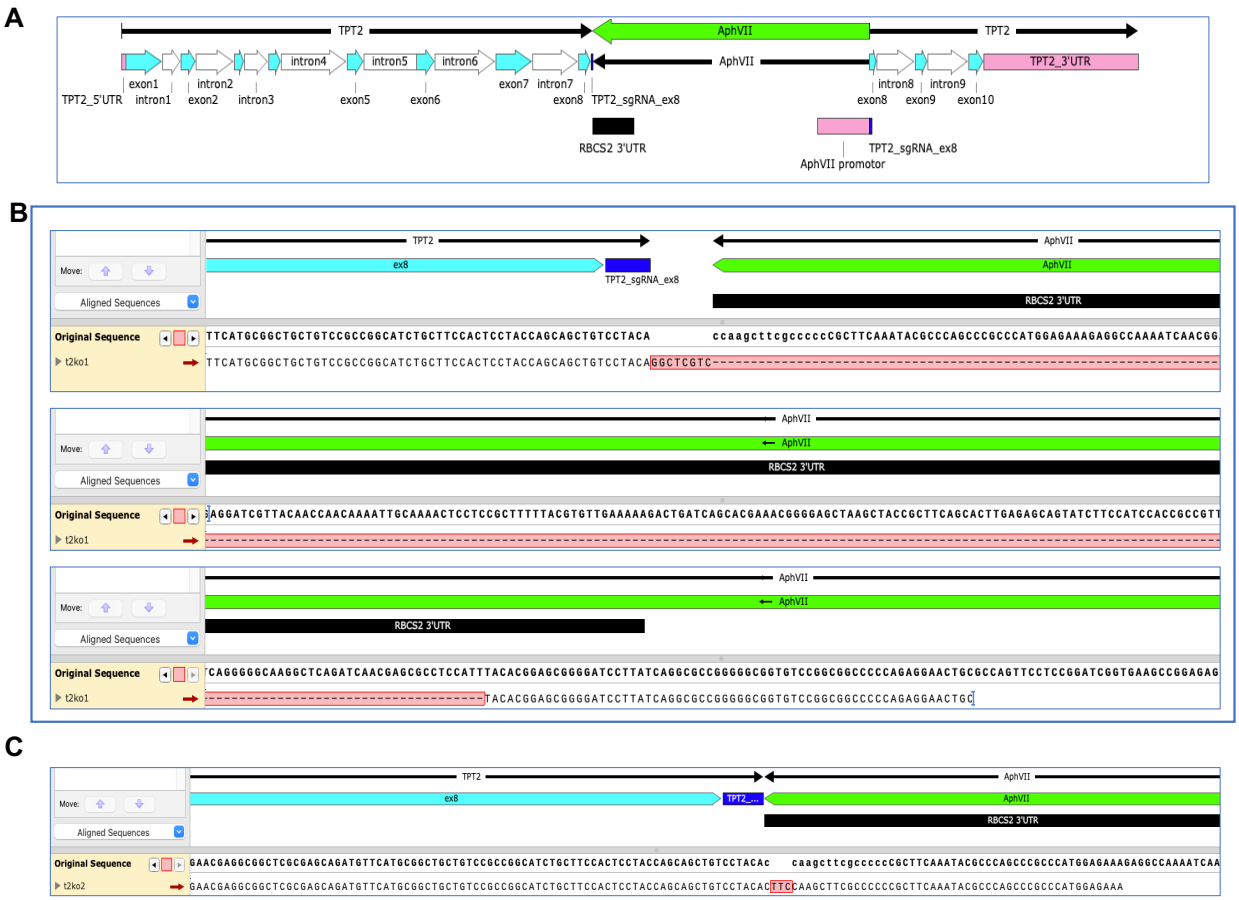

Supplementary Fig. 3: Mutations generated in the Cre*TPT2* gene by CRISPR-Cas9 mediated insertion. (**A**) Presentation of the orientation and position of *AphVII* cassette in the Cre*TPT2* gene in *t2ko1* and *t2ko2*. Sequencing of genomic DNA fragments across the site of *AphVII* cassette in *t2ko1* (**B**) and *t2ko2* (**C**). The mismatched nucleotides are marked in pink. Deletions are shown with dashes.

1367

1368 **Supplementary Fig. 4: Types of mutations generated in the Cre*TPT3* gene by CRISPR-Cas9**
1369 **mediated insertion with sgRNA1 in exon1 and sgRNA2 in exon7.** Sequencing of genomic DNA
1370 fragments across the site of insertion of *AphVII* cassette in *t3ko1* (**A**) *t3ko2* (**B**) and *t3ko3* (**C**). The
1371 orientation and position of *AphVII* cassette are presented above the alignment. The mismatched
1372 nucleotides are marked in pink. Deletions are shown with dashes.

1373

1374

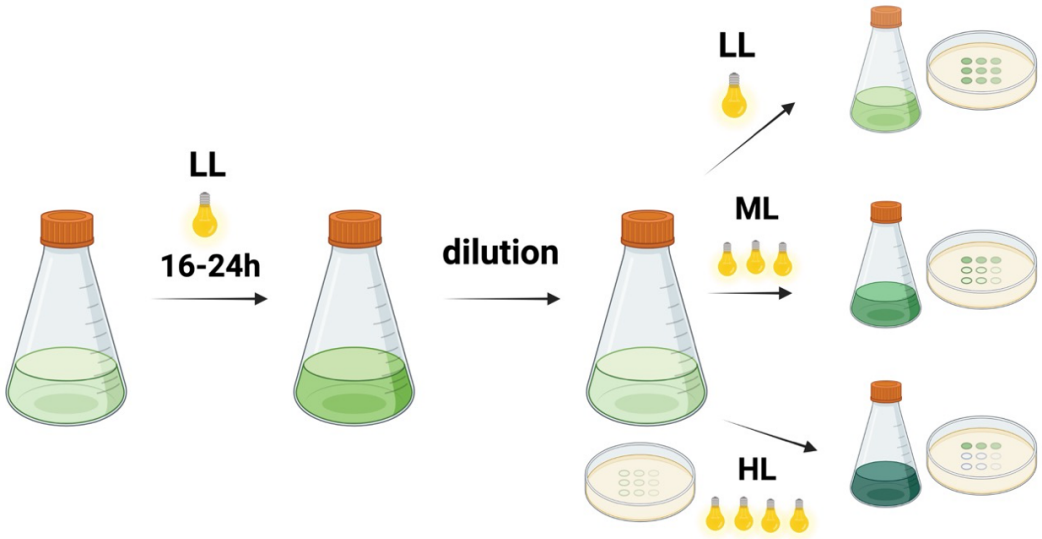

1375

1376 **Supplementary Fig. 5: Experimental set up.** All strains were grown photoautotrophically under low white
1377 light (LL, 30 µmol photons m^{-2} s^{-1}) for 16-24 h. After dilution with fresh medium, the cultures from LL
1378 were then either spotted onto solid medium or to liquid medium and maintained at either LL, moderate light
1379 (ML, 250-300 µmol photon m^{-2} s^{-1}) or high light (HL, 450 µmol photon m^{-2} s^{-1}) for 24 or 48 h. To avoid
1380 self-shading, the culture density was adjusted to 1-1.5 µg/mL chlorophyll before exposure to ML or HL.

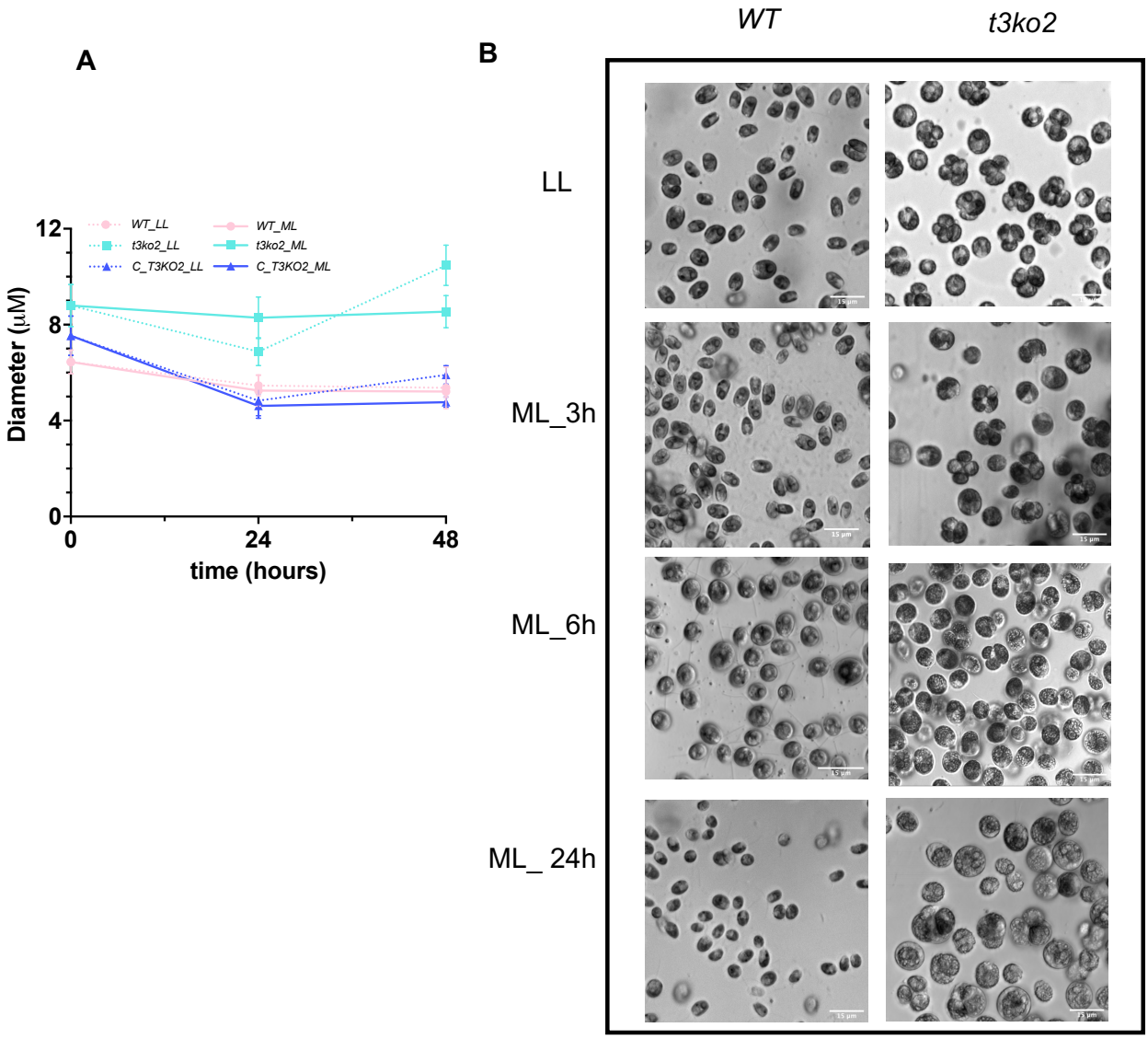

Supplementary Fig. 6: (**A**) Cell size of WT, *t3ko2*, and *C_T3KO2* in TP in both LL and ML. (**B**) WT and *t3ko2* morphology 24 h following a LL to ML transition.

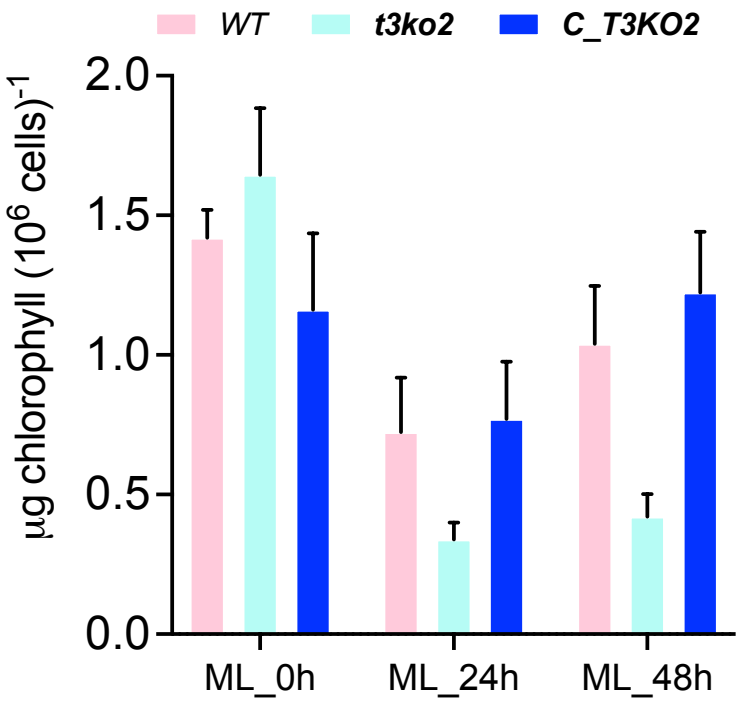

1384

1385 **Supplementary Fig. 7: Quantification of chlorophyll contents in indicated strains after exposure to**
1386 **ML for 24 and 48 h.** All strains were grown photoautotrophically in LL for 16-24 h. After dilution with
1387 fresh medium, the culture was transferred to ML and the chlorophyll content determined after 24 and 48 h
1388 in the ML. The initial inoculum density used for the transition was between 1-1.5 µg/mL chlorophyll in
1389 order to avoid self-shading.

Supplementary Fig. 8: Starch and metabolites in WT and *t3ko2*. (**A**) Starch content in indicated strains following 0, 6, and 24 h in LL. (**B**) Time course, over a period of 6 h, of change in metabolite pool sizes measured at 0 h (LL), 45 min and 6 h after shifting LL-grown cells to ML. Data was normalized to cell numbers. (**C**) Schematic representation of the fold-change for the metabolites shown in (**B**), calculated by dividing the pool size in *t3ko2* by that of WT cells under the same conditions. Fold change of 1 (no change) is shown by a dashed line. Each data point is the mean and standard error of three biological replicates. Asterisk indicates statistically significant differences relative to WT (* P<0.05, ** P<0.01, *** P<0.001). Abbreviations: G6P, glucose-6-phosphate; FBP, fructose bisphosphate; DHAP, dihydroxyacetone phosphate; 3-PGA, 3-phosphoglycerate; PEP, phosphoenolpyruvate; CIT, citrate; SUCC, succinate; FUM, fumarate; MAL, malate; S7P, sedoheptulose-7-phosphate; E4P, Erythrose 4-phosphate; R5P, Ribose 5-phosphate; RU5P/X5P, ribulose 5-phosphate/xylulose-5-phosphate.

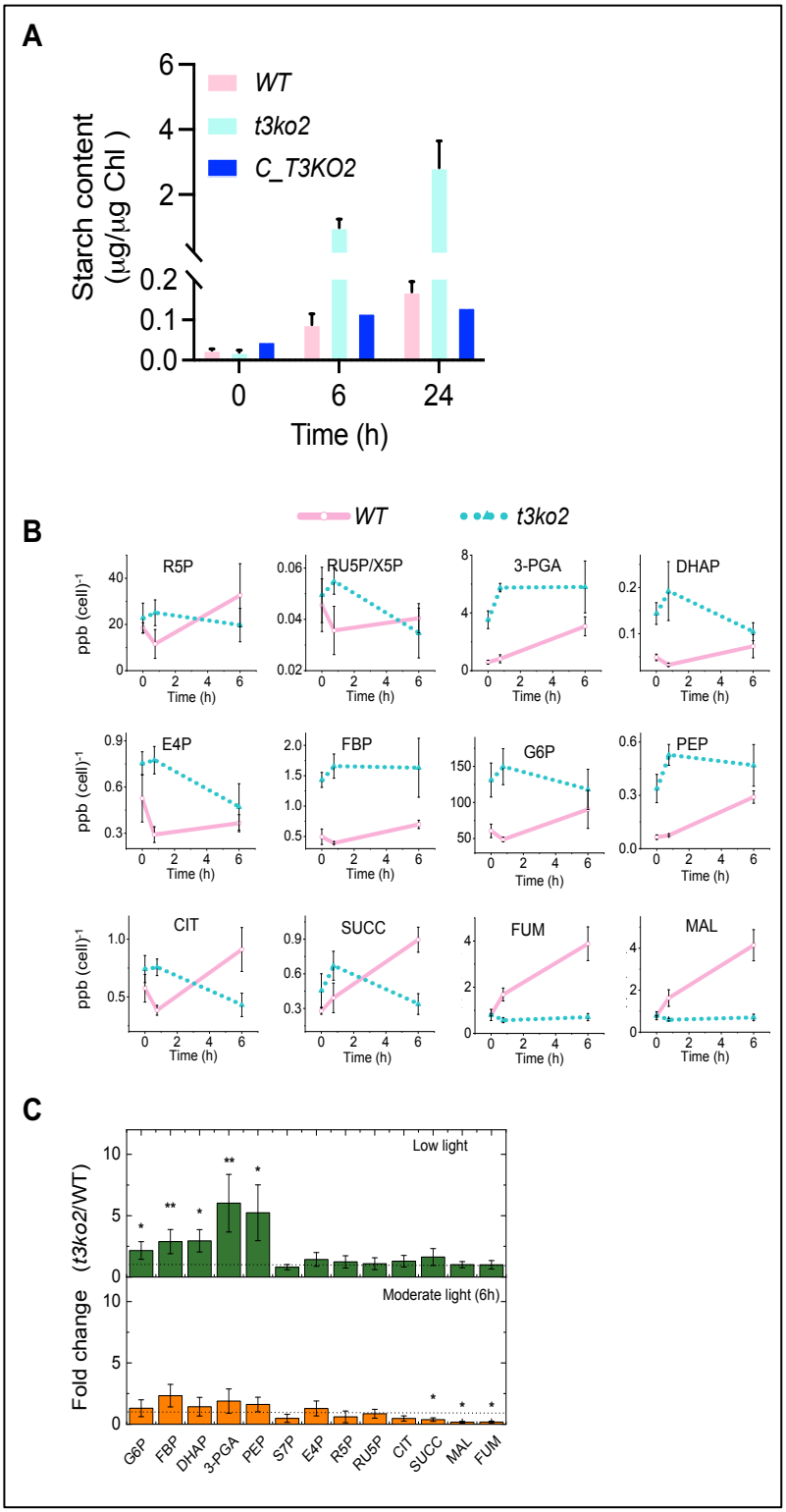

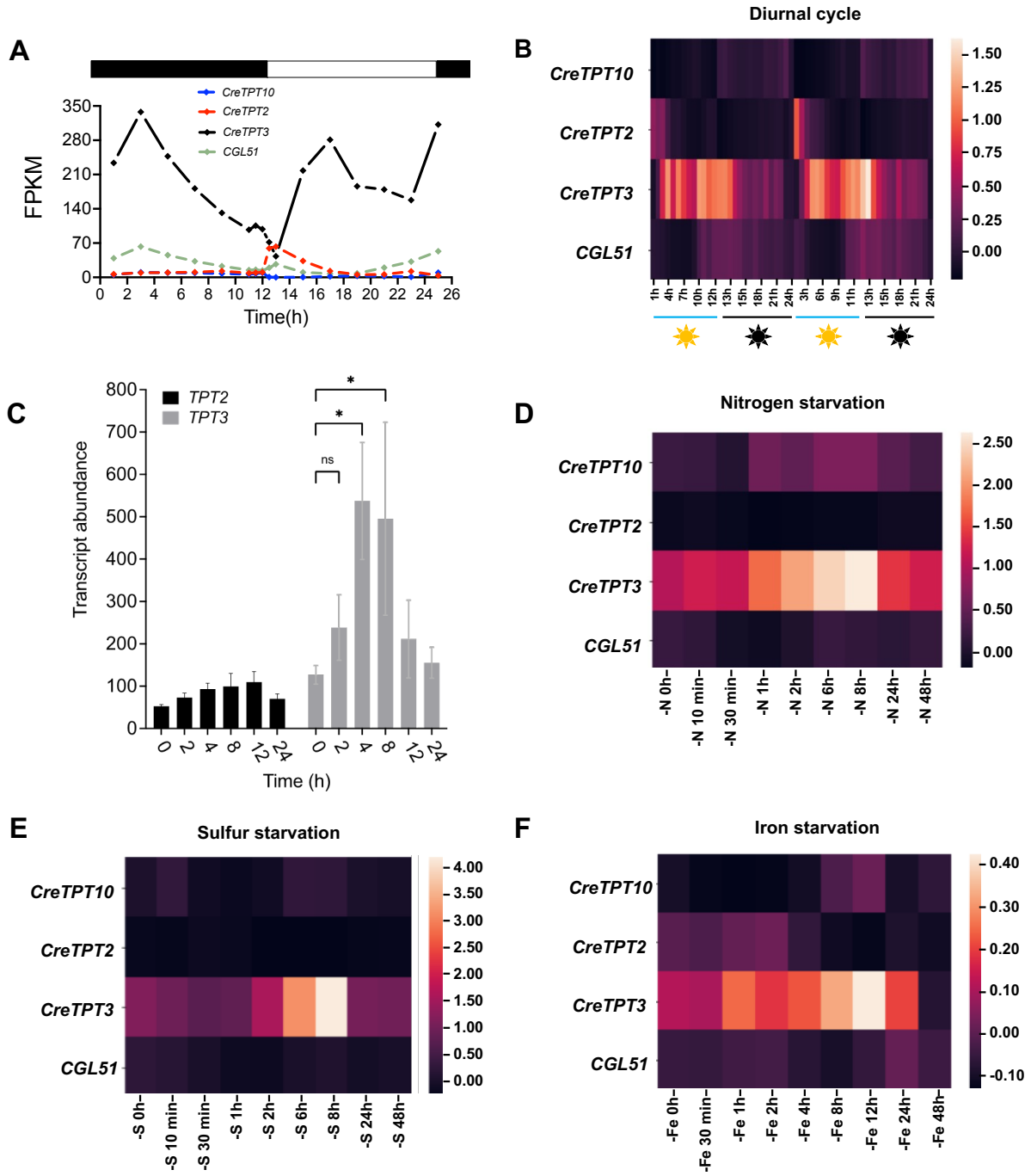

Supplementary Fig. 9: transcript changes of Cre*TPT2* and Cre*TPT3* with various conditions. Histogram (**A**) and heatmap (**B**) of expression of pPTs under diurnal cycle, data was extracted from Zones et al., 2015. **(C)**, Expressions of Cre*TPT2* and Cre*TPT3* following exposure of LL grown cells to HL. Expression of the putative pPTs under nitrogen starvation **(D)**, sulfur starvation **(C)**, and iron starvation **(D)** from (Zones et al., 2015; Ngan et al., 2015; González-Ballester et al., 2010; Urzica et al., 2013).

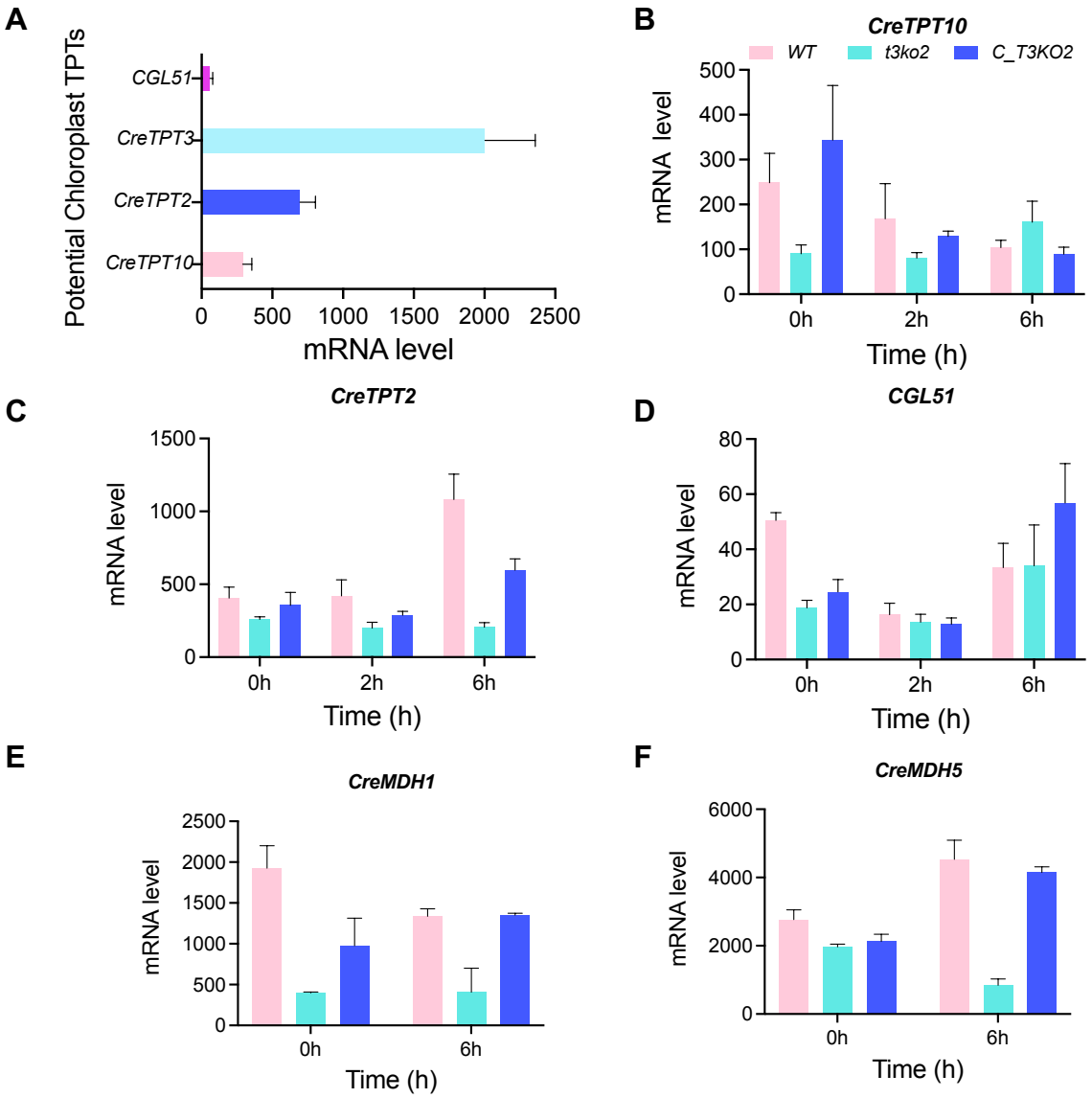

Supplementary Fig. 10: (**A**) mRNA levels encoding putative chloroplast envelope localized pPTs under LL during growth in TP medium. mRNA levels of Cre*TPT10* (**B**), Cre*TPT2* (**C**) and *CGL51* (**D**) in the indicated strains 0, 2, 6 h after the cells were shifted from LL to ML. (**E, F**) mRNA levels of plastidial malate dehydrogenases (*MDH*) in the indicated strains 0, 6 h after the cells were shifted from LL to ML.

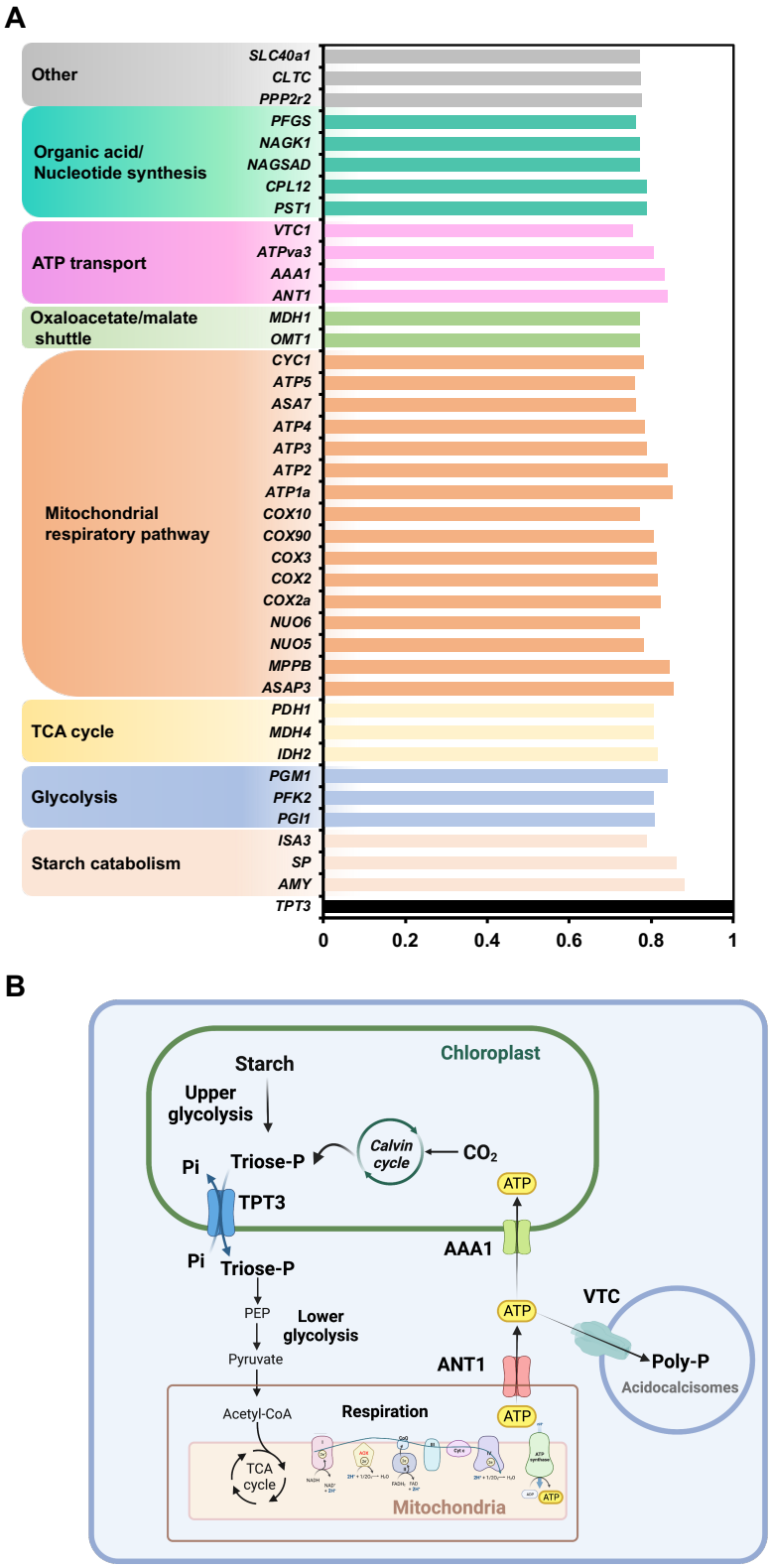

1429 **Supplemental Fig 11: List of genes with strong correlation relative to Cre*TPT3*.** (**A**) Correlation
1430 coefficients greater than 0.75 were listed. (**B**) Construction of Cre*TPT3* co-expression networks.